

Mechanical Properties of Ionic Self-Complementary Oligopeptide Biomaterials

by

Erasmus J. León

B.A. Mathematics
Saint Louis University, 1993

B.S. Mechanical Engineering
Georgia Institute of Technology, 1995

Submitted to the Department of Mechanical Engineering
in partial fulfillment of the requirements for the degree of

Master of Science in Mechanical Engineering

at the

MASSACHUSETTS INSTITUTE OF TECHNOLOGY

June 1997

© Massachusetts Institute of Technology 1997. All rights reserved.

Author (Department of Mechanical Engineering
May 9, 1997

Certified by
Roger D. Kamm
Professor of Mechanical Engineering
Thesis Supervisor

Accepted by.....
Ain A. Sonin
Professor of Mechanical Engineering
Chairman, Departmental Committee on Graduate Studies

MASSACHUSETTS INSTITUTE
OF TECHNOLOGY

JUL 21 1997

Eng.

Mechanical Properties of Ionic Self-Complementary Oligopeptide Biomaterials

by

Erasmio J. León

Submitted to the Department of Mechanical Engineering on May 9, 1996,
in partial fulfillment of the requirements for the degree of
Master of Science in Mechanical Engineering

Abstract

The materials used in medical science are a primary area of research in the development of tissue engineering therapies. There is an urgent need for a great number of materials that can meet the wide range of requirements imposed by biomedical applications. Ionic self-complementary oligopeptide biomaterials are a new class of synthetic materials with great potential for medical use. The objective of this research was to characterize the structure and mechanical properties of a member of this class of materials, EFK8.

The structure of EFK8 was studied using scanning electron microscopy. The peptide materials exhibited a fibrous structure. Similar fibrous networks were observed in two other oligopeptide materials, RADA16 and RFE8. The micrographic analysis allowed the determination of key structural features such as fiber thickness and mean fiber length. At a concentration of 3.3 mg/ml, EFK8 exhibited fibers of approximately 11.4 to 22.4 nm in thickness and 186 nm in length. The matrix relative density, which gives the ratio of matrix density to fiber density, was calculated to be between 0.01 and 0.04. A higher concentration, namely 10 mg/ml, resulted in a shorter fiber length of 73 nm and a higher relative density of 0.07 to 0.16.

The tensile properties of EFK8 were characterized using a small-scale testing system. Data from tensile tests were used to generate stress-strain curves of the material. Results show that the material exhibits an elastic-brittle behavior. Its mechanical properties are strongly dependent on peptide concentration. The theory of cellular solids was used to model the dependence of the material's Young's modulus, strength, and elongation on concentration. The Young's modulus and the strength of EFK8 increased

with increase in concentration. The elongation, on the other hand, decreased with increased concentration. These trends were in agreement with cellular solid theory predictions. The tested concentrations of EFK8 ranged from 2.7 to 10 mg/ml. These concentrations gave Young's modulus ranging from 1.59 to 15.4 kPa. The ranges for fracture strength and the elongation were 50.5 to 196.5 Pa and 1.2 to 5.9%, respectively. Predicted values of fibers' Young's modulus, based on cellular solid theory, are 0.56 to 22.8 MPa.

Thesis Supervisor: Roger D. Kamm
Title: Professor of Mechanical Engineering

Acknowledgments

I would like to thank the many individuals who assisted me in the completion of this project. I first wish to thank Roger Kamm for giving me the opportunity to work on this project and providing continuous advice and support. Many thanks to Shuguang Zhang for his enthusiasm and his patience in guiding me through all the Biochemistry-related issues of the project. I also thank Doug Lauffenburger for his interest and valuable suggestions.

I wish to thank Gabriela Krockmalnic for her assistance in the preparation of specimens for scanning microscopy. Many thanks to David Bell for his assistance in the attainment of the scanning electron micrographs.

I wish to thank the students of the Fluid Mechanics Lab for their support and diversionary conversations.

I especially thank my family for their motivation, support, and encouragement. Thanks to my parents for giving me the strength to set my sight on high goals and see them through completion despite the many obstacles.

Thanks to all the people who have believed in me and have given me the chance to achieve my goals.

Contents

Abstract	2
Acknowledgments	4
Contents	5
List of Figures	7
List of Tables	8
1. Introduction	9
1.1 Overview	9
1.2 Objectives	10
1.3 Thesis Outline	10
1.4 References	12
2. Background	13
2.1 Introduction	13
2.2 Tissue Engineering	13
2.3 Biomaterials	16
2.3.1 Natural and Synthetic Biomaterials	18
2.3.2 Summary	19
2.4 References.....	20
3. Ionic Self-Complementary Oligopeptide Biomaterials.....	21
3.1 Introduction	21
3.2 Ionic Self-Complementary Oligopeptides	21
3.2.1 Background	21
3.2.2 Amino acid Composition of Oligopeptides	26
3.2.3 Properties	29
3.3 EFK8	30
3.4 References	34
3.A Picture of Macroscopic Oligopeptide Matrices	35
4. Structural Analysis with Scanning Electron Microscopy	36
4.1 Introduction	36
4.2 Specimen Preparation	36
4.3 SEM Imaging.....	37
4.3.1 Micrographs	37
4.3.2 Results	37

4.3.3 Image Analysis	43
4.3.4 Discussion	46
4.4 References	49
4.A Preparation of Biological Samples for SEM Studies	50
4.B Derivation of Mean Length Correction Factor	54
5. Mechanical Testing	56
5.1 Introduction	56
5.2 Background	56
5.3 Mechanical Testing Device	58
5.3.1 System Description	58
5.3.2 Specifications	60
5.4 Diffusion-Controlled Assembly Model	61
5.4.1 Peptide Matrix Fabrication Process	61
5.4.2 Diffusion Model	62
5.4.2A Model 1: Graetz Problem	62
5.4.2B Model 2: Two-Region Diffusion	64
5.5 Tensile Test Results	69
5.4 References	76
6. Cellular Solid Analysis	77
6.1 Introduction	77
6.2 Background	77
6.3 Analysis	80
6.4 Discussion	85
6.5 References	89

List of Figures

Figure 3.1	Amino acid components of EAK oligopeptides	22
Figure 3.2	Schematic of weak interactions in peptides.....	24
Figure 3.3	Proposed model for peptide assembly	28
Figure 3.4	Chemical structure of EFK8 components and peptide	32
Figure 3.5	Molecular model of EFK8.....	33
Figure 4.1	SEM's of EFK8 at 3.3 mg/ml.....	39
Figure 4.2	SEM's of RADA16 at 2 mg/ml.....	40
Figure 4.3	SEM's of EFK8 at 10 mg/ml.....	41
Figure 4.4	SEM's of RFE8 specimen	42
Figure 4.5	SEM's of EFK8 at 3.3 mg/ml used for image analysis	45
Figure 5.1	Schematic of tensile testing system.....	59
Figure 5.2	Picture of tensile testing system	59
Figure 5.3	Picture of tensile test specimens.....	61
Figure 5.4	Fabrication of oligopeptide matrix	62
Figure 5.5	Peptide matrix fabrication diffusion model: Graetz problem.....	63
Figure 5.6	Diffusion models comparison.....	67
Figure 5.7	Effect of outer radius in model prediction.....	68
Figure 5.8	Averaging strain technique for stress-strain curves.....	72
Figure 5.9	Tensile stress-strain curves for EFK8 at 2.7 mg/ml	72
Figure 5.10	Tensile stress-strain curves for EFK8 at 3.3 mg/ml	73
Figure 5.11	Tensile stress-strain curves for EFK8 at 5.4 mg/ml	73
Figure 5.12	Tensile stress-strain curves for EFK8 at 10 mg/ml	74
Figure 6.1	Unit cell model	78
Figure 6.2	Young's moduli dependence on concentration: linear scale	82
Figure 6.3	Young's moduli dependence on concentration: logarithmic scale.....	82
Figure 6.4	Fracture strength dependence on concentration: linear scale	84
Figure 6.5	Fracture strength dependence on concentration: logarithmic scale.....	84
Figure 6.6	Elongation at fracture dependence on concentration: linear scale.....	86
Figure 6.7	Elongation at fracture dependence on concentration: logarithmic scale	86

List of Tables

Table 1.1 Objectives	10
Table 2.1 Summary of Biomaterials' Properties	19
Table 3.1 Non-Covalent Interactions in Biomolecules	25
Table 4.1 Image Analysis Results: EFK8	46
Table 5.1 Tensile Tests Data for EFK8	71
Table 6.1 Fiber Modulus Results: EFK8	81

Chapter 1

Introduction

1.1 Overview

Treatment of organ and tissue damages presents a prominent challenge in today's health care system. Every year millions of Americans seek medical care for this type of disorders. The urgent need for effective therapies to deal with these ailments has given rise to the field of tissue engineering. In this field, scientists attempt to repair damaged tissue and organs with functioning lab-grown substitutes. Tissue engineering offers attractive alternatives to current important medical procedures like organ transplantation. The techniques used in tissue engineering eliminate the problems of donor shortage and immunorejection of implants, which impose significant limitations to transplants.

The materials used for biomedical applications are presently a focal area of research and present one of the main challenges in tissue and medical-device engineering (1, 2). New biomaterials are continuously developed and improved to try to meet the many challenges imposed by tissue engineering and clinical intervention. These materials must address a wide range of needs requiring different biological and physico-mechanical properties. A detailed characterization of these properties is necessary for the successful use of materials in medicine.

Ionic self-complementary oligopeptide biomaterials are a new class of synthetic materials with great potential for medical use. These oligopeptides are composed of natural amino acids and are able to self-assemble into macroscopic matrices (3, 4). The resulting matrices, which are biochemically and biophysically stable, are biodegradable and can support cell attachment (3, 5). Therefore, they could potentially be developed for biomedical applications as scaffolds for cells, wound dressings, or tissue adhesives.

In order to determine the viability of the peptide matrices for medical applications, their properties must be determined. This research is concerned with their mechanical properties. A better understanding of the materials' mechanical properties will help identify particular medical applications for which they are suited. To gain some of this knowledge, tensile tests were performed on members of the new class of biomaterials. The materials' microstructure was characterized using scanning electron microscopy. The theory of cellular solids was then used to study the relationship

between microstructure and matrix tensile properties as well as their dependence on material concentration.

1.2 Objectives

The goal of this research was to develop methods for the characterization of the structure and mechanical properties of ionic self-complementary oligopeptide biomaterials. The material selected for this study was EFK8. It was intended to establish the methodology for fabricating material specimens and testing them under tensile load. The data obtained would be used to produce stress-strain curves characterizing the material's mechanical behavior under tension. Parameters to be determined from these data included the Young's modulus, the fracture strength, and the strain to failure. It was also intended to establish a method for determining the material's structure. Using scanning electron microscopy, parameters such as fiber size and pore size would be measured. This data could be used to establish material properties like solid volume fraction. The effect of material concentration on its structure and tensile properties was to be determined with the help of the theory of cellular solids. The main objectives are summarized on Table 1.1.

Table 1.1 Objectives

<ol style="list-style-type: none">1. Develop methodology for specimen preparation and tensile testing2. Perform tensile tests on peptide material3. Develop methodology for structural characterization4. Determine material micro-structure5. Establish concentration effects in structure and mechanical properties

1.3 Thesis Outline

Many recent developments in tissue engineering and medical intervention are due to notable advances in the development of new biomaterials. Chapter 2 presents background information on the most significant techniques used on tissue engineering. It also discusses the properties and requirements for materials used in tissue and organ repair. It also describes some of the biomaterials frequently used in medicine.

Chapter 3 includes background information on ionic self-complementary oligopeptides. The chapter explains their composition and self-assembly properties. It also discusses how its biomedical properties make it an attractive material for medical applications. The chapter ends with a description of EFK8, the material used in this research.

The structural analysis of the biomaterials is presented on Chapter 4. This chapter describes use of scanning electron microscopy in determining the fibers' thickness and their separation distances. It also presents the use of this information in obtaining the solid volumetric fraction, or relative density.

Chapter 5 discusses the material's tensile testing. It describes the apparatus and methodology used for specimen fabrication and testing. The fabrication methodology includes a model of the diffusion-controlled assembly process. The chapter presents the tensile test results for EFK8 matrices fabricated from different concentrations.

An analysis of how the mechanical properties relate to the structural properties is included in Chapter 6. This chapter includes an analysis based on the theory of cellular solids. Using this theory, the matrix mechanical and structural properties can be used to predict the properties of the solid fibers in the matrix. It also allows determination of the properties at various concentrations. The results from this analysis for EFK8 are presented and discussed in this chapter.

1.4 References

1. Kohn, J. "Tissue Engineering: An Overview," *MRS Bulletin*, November 1996, pp. 18-19.
2. Langer, R. and J.P. Vacanti. "Tissue Engineering," *Science*, Vol. 260, May 1993, pp. 920-926.
3. Zhang, S., T. Holmes, C. Lockshin, and A. Rich. "Spontaneous Assembly of a Self-Complementary Oligopeptide to Form a Stable Macroscopic Membrane," *Proceedings of the National Academy of Science USA*, Vol. 90, pp. 3332-3338, 1993.
4. Zhang, S., C. Lockshin, R. Cook, and A. Rich. "Unusually Stable Beta-Sheet Formation in an Ionic Self-Complementary Oligopeptide," *Biopolymers*, Vol. 34, pp. 663-672, 1994.
5. Zhang, S., T.C. Holmes, C.M. DiPersio, R.O. Hynes, X. Su, and A. Rich. "Self-Complementary Oligopeptide Matrices Support Mammalian Cell Growth," *Biomaterials*, Vol. 16, pp. 1385-1393, 1995.
6. Gibson, L.J. and M.F. Ashby. *Cellular Solids: Structure and Properties*, New York: Pergamon Press, 1988.

Chapter 2

Background

2.1 Introduction

The damage and failure of human tissues and organs represent an overwhelming challenge in health care. The search for new ways to ameliorate this problem has given rise to the rapidly emerging field of tissue engineering. Scientists in this field attempt to reconstruct damaged tissue with substitutes fabricated in the laboratory. Many of the recent advances in this field are primarily due to the development of reprocessed biological materials and synthetic polymers used in tissue and organ replacement. There is an urgent need and a great demand for new materials that can cover a wide range of applications in the field while taking into consideration relevant issues such as bioresorbability, biocompatibility, and minimal immunogenicity.

This chapter presents a summary of some of the recent advances in tissue engineering. Then, it reviews the properties, characteristics, and applications of some of the materials currently used or studied in the field.

2.2 Tissue Engineering

Tissue and organ failure can have seriously adverse effects on the health of an individual. They are among the major challenges in today's health care system. Every year these disorders affect millions of Americans. The number of surgical procedures performed annually in the United States to treat tissue and organ damage approximate 8 million (5). Many of the diseases resulting from the damage are treated by organ and tissue transplantation. Transplantation therapies depend on the availability of donor tissue and organ. Donor supply is very limited and, thus, insufficient for the large number of patients requiring treatment. For instance, 30,000 people died from liver tissue failure in 1989 while only 2160 donor livers were available for transplant (2). A similar shortage of cartilage tissue affects over 1 million patients requiring cartilage replacement in the United States every year (1). These problems have motivated scientists to search

for alternative therapies for tissue and organ damage, leading to the emergence of tissue engineering.

Tissue engineering is a rapidly growing field that combines knowledge from the disciplines of biology, engineering, and materials science. It uses the principles from these fields to develop tissues and materials that serve as functional replacements or assist in the repair of damaged tissues and organs. Examples of replacement/repair substitutes include scaffolds for tissue regeneration, surgical sutures, bone fracture fixation devices, wound dressings, and bioadhesives. The use of such therapeutical materials presents an attractive alternative to transplantation. These artificial substitutes are less expensive than donor organs and tissues and are readily available. Furthermore, they allow intervention and repair before critically ill stages that require removal and replacement of damaged organ or tissue.

Cell transplantation has been proposed as a promising alternative to transplantation for tissue repair and organ replacement. Its potential use in tissue reconstruction make it an ideal candidate for the treatment of ailments due to enzyme deficiencies such as liver disease, hemophilia, and Parkinson's disease as well as to the damage of a variety of tissues including skin and cartilage (2). This therapy consists of implanting dissociated cells that are supported on a polymeric matrix. The matrix, also known as scaffold, provides a mechanical support that allows the seeded cells to organize and generate new tissue. The cell-scaffold construct is prepared in vitro and then transferred into the patient, where the new organ or tissue will be formed. As the new tissue is formed, cells will synthesize the proteins that form the extracellular matrix. This extracellular matrix will replace the degrading scaffold in providing the mechanical support for the cells. An alternative method uses tissue islets encapsulated in a semipermeable material. These capsules can be injected rather than surgically implanted into the patient (1). One of the earliest implementations of these techniques was achieved in 1933 by Vincenzo Bisceglie in Italy. Bisceglie inserted mouse tumor cells in the abdominal cavity of a guinea pig by encapsulating them in nitrocellulose (1).

The success of cell-scaffold constructs results from the tendency of isolated cells to reconstruct the appropriate tissue structure and of tissues to undergo remodeling (5). In spite of that tendency, the self-organization and tissue forming ability of cells is quite limited. Dissociated cells require a template that guides their organization and growth (5). That template is usually provided by the supporting existing polymeric scaffold. The capability of cells to organize into functional tissues under appropriate conditions is what makes cell-based transplantation attractive. The technique can be used to allow the incorporation of healthy cells into a damaged area of an organ, thus accelerating repair

and eliminating the need to replace the whole organ. Tissue repair with cell-scaffold constructs has so far been used in a limited variety of tissues including bone, cartilage, and ligaments. Since the technique requires only part of a tissue, several patients can be treated with the tissue from a single organ, eliminating the problem of donor shortage.

Other examples of applications of tissue reconstruction are in the areas of soft-tissue closure and accelerated wound healing. Scientists in these areas are interested in the development of new biomaterials that can assist or promote better tissue healing. One example of the use of these materials is in the fabrication of surgical sutures. Various synthetic polymers such as polylactic acid have been widely used as suture materials for wound-closure as well as fixations of tendons, ligaments, and bone fractures (7, 13). Another application is in the preparation of wound dressings. The dressings are coatings that assist the treatment and healing of deep wounds, burns, and other injuries. They help in preventing infection, impeding fluid loss, and preventing scar-tissue formation. One of such dressings, developed by Genzyme, in Cambridge, Massachusetts, is made with hyaluronic acid. It is used after surgery to prevent the adhesion of scar-tissue between organs (1). Some approaches used in the reconstruction of damaged skin combine the use of a dressing with cell transplantation. For instance, a coating with a thin layer of a collagen based biomaterial in direct contact with tissue and an upper layer of silicone is applied to the patient (5). The collagen in contact with the skin promotes tissue ingrowth while the silicone prevents fluid loss. After several weeks, the silicone is removed and an epidermal tissue graft is implanted.

A large variety of biomaterials are used in applications as bioadhesives and controlled-drug release devices. Most of the materials used in these fields are resorbable, eliminating the need of additional surgery for removal. Degradable adhesive polymeric materials such as fibrin glues, cyanoacrylates and polyphosphates serve in diverse applications as bone cements, covers, and sealants (7). Biomaterials are largely used for controlled delivery of drugs. Drugs are incorporated into a polymeric mesh or gel that is implanted into the host. The drugs will then be released by diffusion into a localized area. Applications of the technique include release of antibiotics for treating bone and wound infections (7). Biodegradable polymers show great potential for temporary fixation of orthopedic prosthetic devices. In such applications they would serve as adhesive and at the same time provide localized release of drugs to prevent infections (7).

2.3 Biomaterials

The success of a large number of techniques in tissue engineering and medical intervention depend strongly on the availability of a large variety of biomaterials. Applications ranging from bone fixation screws to hydrogels for wound dressings require materials displaying a wide range of properties. Those materials must answer different needs in terms of surface chemistry, mechanical properties, and physical characteristics. They must also address issues related to the patient's health such as immunogenicity, secondary effects and biodegradability.

In order to meet the demands of biomaterial properties, scientists have explored and developed a large number of materials for the many applications of tissue engineering. Synthetic polymers as well as reprocessed natural materials have been studied and used with some success in various applications. Whether a synthetic material or a natural material is more appropriate will be dictated by the function intended for it and the type of tissues involved. However, each type has some intrinsic advantages over the other. For instance, natural materials contain information that is important in promoting and optimizing various types of advantageous cell interaction like adhesion (5, 8). A disadvantage of natural materials is that their antigenicity may elicit adverse immunological responses (8). Furthermore, the batch-to-batch variability of natural materials hinders the desired controllability of properties (5). Synthetic materials lack the intrinsic information of natural materials, but possess the advantage of easy controllability of attributes such as weight and degradation rate (5).

A better understanding of the properties of biomaterials and how these affect the tissue reconstruction activity is required before tissue engineering can become a common treatment method. A great deal is to be learned about the specific criteria that must be met by materials used for the various applications in tissue engineering. However, some of the basic design criteria for the materials and structures used as cell scaffolds in has been established. First, the material surface should interact favorably with the cells to allow cell adhesion and growth (6). The material should exhibit long term tissue biocompatibility (1, 2, 6). This requirement dictates that the material should provoke minimal harmful interaction with living cells so that the tissue remains functional. In addition, the material must be easily processable (6). In other words, the material should be reproducibly formable into scaffolds of different geometries, as specified by the desired resulting tissue structures. The resulting scaffold should be highly porous (2). First, this ensures a high surface area to volume ratio. The high surface area provides optimal space for cell-material interaction (2). Second, large pores allow for vascularization of the graft . As a result, the blood supply for the transport of cellular

nutrients and wastes will be developed (2). It has been observed that porosities higher than 90% are required (6). The minimum pore size required for vascularization is about 60 microns (2). A final requirement for the scaffold material is that it should be resorbable (6). The material should degrade after it has completed its function, eliminating the possibility of long-term problems. The degradation products should not present adverse effects to the new tissue or the host.

The various biomedical applications also impose specific requirements of physico-mechanical properties including mechanical, thermal, and degradation characteristics on biomaterials. A recent literature review revealed a lack of detailed investigation and availability of reliable data of these properties (13). As a result of the absence of biomechanical data on living tissues and biomaterials, most of the available artificial organs are not optimally designed (14). Of great importance are the mechanical properties such as elastic modulus and tensile strength. Biomedical materials must withstand the loads acting on them without failing and preventing the normal functioning of the tissues being treated or regenerated. For instance, the high loads experienced by bones and connective tissues will require the use of high strength materials like aliphatic polyesters for orthopaedic implants. Materials used for wound dressings would be exposed to mechanical insults that impose minor loads on the material or tissue under treatment. Therefore, those materials are not required possess high strength properties needed for orthopaedic devices. In the case of cell scaffolds, the matrices must have the mechanical strength to support the growth of cells for prolonged periods. The mechanical properties of scaffold materials play an important role in tissue regeneration kinetics. A model of the effects of mechanical forces on cell shape and function, known as the “tensegrity” model, predicts that the substrate’s mechanical properties determine whether cells differentiate or proliferate (6). It states that rigid substrates induce proliferation while malleable ones induce differentiation (6). Mechanical compatibility between biomaterials and tissues is critical in the design of implants (14). A mismatch in the mechanical properties of the natural tissues and the implant materials could seriously affect functionality. Large differences in properties result in high concentrations of stress and strain at attachment sites, leading to material failure and implant malfunction (14). For instance, mechanical mismatch between vascular grafts and host arteries causes flow disturbances and stress concentrations leading to failure of suture, local thrombus formation, and other complications (14).

2.3.1 Natural and Synthetic Biomaterials

A large number of materials used in medicine and tissue engineering are derived from natural macromolecules such as polysaccharides and proteins. These materials contain information that promote cell activities and do not present the severe toxicity problems usually associated with synthetic polymers. One example is the cellulose derivative used in an FDA approved fabric sheet developed by Johnson and Johnson Medical. The sheet used as a wound dressing adheres to wounded tissue and forms a hydrogel coating as it degrades (2).

One of the natural materials most frequently used for biomedical applications is collagen. Reprocessed collagen in its various physical forms has been investigated for clinical applications that include bone-cartilage substitute, vascular grafts, and wound dressings (10). For instance, collagen fibers made from catgut have been used as suture material since the last century (7). Collagen is a major component of tendon and connective tissue. Its mechanical properties, characterized by low extensibility and high tensile strength, make it extremely attractive for implant material. Wet collagen tendon has a Young's modulus of 2 GPa and exhibits tensile strength of 60 to 100 MPa and elongation to fracture of 5 to 10% (8, 9). The various physical forms of reprocessed collagen show different properties and, as a result, different applicability in medical therapies. Collagen reconstituted into a sponge or felt-like material has been developed for use as a wound and burn dressing, intravaginal contraceptive, and tampons (10, 11). This collagen-sponge fabricated from a 0.5 - 2% aqueous slurry has a tensile modulus of approximately 2.5 kPa (10). Cross-linking the sponge with an aldehyde as a tanning agent increases its modulus to 20 kPa (10). Collagen fibers have been used as suture materials and woven into meshes for vascular grafts (12). Continuous fibers made by an automated extrusion process were shown to have tensile moduli of 3.6 MPa when uncross-linked and 270 MPa when cross-linked (11). Tanning of collagenous materials with aldehydes increases their tensile strength and modulus, stability, and rate of degradation (2, 10, 8, 12). However, long-term implants of highly tanned collagen can cause problems such as immunogenicity and fibrous scarring (2).

Degradable synthetic polymers have been used extensively for medical applications for decades. The ease of properties controllability and processability have made their commercial applicability and availability for clinical use feasible. The most commonly used polymers are the aliphatic polyesters polylactic acid (PLA), polyglycolic acid (PGA), and their copolymers like PGLA. Their uses include surgical sutures, cell scaffolds, and bone-fixtured devices. PGA surgical sutures, commercially known as Dexon™, are approved by the Food and Drug Administration and have been available

since 1970 (13). The high stiffness of these polyesters make them extremely useful for load bearing applications. PLA and PGA show tensile moduli of 2-10 GPa and 6.5 GPa, respectively (4, 7). These materials are also used to make porous matrices for cartilage repair and growth. A mesh with porosity of 97% has been used to generate *in vitro* chondrocyte-PGA construct 1 cm in diameter and 0.35 cm in thickness (6). A disadvantage of polyesters is their release of acidic-degradation products which present biocompatibility difficulties.

2.3.2 Summary

A summary of the applications and mechanical properties of various biomaterials is included in Table 2.1. References are indicated in parenthesis.

TABLE 2.1. Summary of Biomaterials' Properties

Material	Young's Modulus	Tensile Strength	Elongation at Fracture	Applications
PLA (4, 7, 13)	2-10 GPa	28-50 MPa	2-6 %	- surgical sutures, bone fixation devices, cell scaffolds
PGA (4,7)	6.5 GPa	47 MPa		- surgical sutures, bone fixation devices, cell scaffolds
polyethylene (15)	410-1240 MPa	23-40 MPa	400-500%	- polymeric joints
collagen:				
-tendon wet (8,9)	2 GPa	60-100 MPa	5-10 %	
-sponge 0.5-2% (10,11)	2.5-20 kPa	-	-	- wound and burn dressings, intravaginal contraceptive, tampons
-thread (12)	3.6-13.2 MPa	-	22-24%	- sutures, vascular grafts

2.4 References

1. Hubbell, J. A. and R. Langer. "Tissue Engineering," *Chemical & Engineering News*, March 13, 1995, pp. 42-54.
2. Cima, L.G., J.P. Vacanti, C. Vacanti, D. Ingber, D. Mooney and R. Langer. "Tissue Engineering by Cell Transplantation Using Degradable Polymer Substrates," *Journal of Biomechanical Engineering*, Vol. 113, 1991, pp. 143-150.
3. Kohn, J. "Tissue Engineering: An Overview," *MRS Bulletin*, November 1996, pp. 18-19.
4. James, K. and J. Kohn. "New Biomaterials for Tissue Engineering," *MRS Bulletin*, November 1996, pp. 20-26.
5. Langer, R. and J.P. Vacanti. "Tissue Engineering," *Science*, Vol. 260, May 1993, pp. 920-926.
6. Freed, L.E., G Vunjak-Novakovic, R.J. Biron, D.B. Eagles, D.C. Lesnoy, S.K. Barlow and R. Langer. "Biodegradable Polymer Scaffolds for Tissue Engineering," *Bio/Technology*, Vol. 12, July 1994, pp. 689-693.
7. Zhang, X. and M.F.A. Goosen. "Biodegradable Polymers (Orthopedic Applications)," *Polymeric Materials Encyclopedia*, Vol. 1, 1996, pp. 593-599.
8. Murabayashi, S., H. Kambic, and Y. Nose. "Reprocessed Biological Materials," *Encyclopedia of Material Science and Engineering*, Vol 6., 1986, pp. 4171-4178.
9. Calvert, P.D. "Biological Macromolecules," *Encyclopedia of Material Science and Engineering*, Vol. 1, 1986, pp. 327-339.
10. Chvapil, M. "Collagen Sponge: Theory and Practice of Medical Applications," *Journal of Biomedical Materials Research*, Vol. 11, 1977, pp. 721-741.
11. Chvapil, M. "Considerations on Manufacturing Principles of a Synthetic Burn Dressing: A Review," *Journal of Biomedical Materials Research*, Vol. 16, 1982, pp. 245-263.
12. Kato, Y.P. and F.H. Silver. "Formation of Continuous Collagen Fibres: Evaluation of Biocompatibility and Mechanical Properties," *Biomaterials*, Vol. 11, 1989, pp. 169-182.
13. Engelberg, I. and J. Kohn. "Physico-mechanical Properties of Degradable Polymers Used in Medical Applications: A Comparative Study," *Biomaterials*, Vol. 12, 1991, pp. 292-304.
14. Hayashi, K. "Mechanical Properties of Biomaterials: Relationship to clinical approach," *Contemporary Biomaterials*, New Jersey: Noyes Publications, 1984, pp. 46-65.
15. Lawrence-Katz, J., L.L. Latta, S. Singh, and H.S Yoon. "Biomechanics of Orthopedics and Rehabilitation of the Musculoskeletal System," *Handbook of Biomedical Engineering*, New York: Harcourt Brace Jovanovich, pp. 460-524, 1985.

Chapter 3

Ionic Self-Complementary Oligopeptide Biomaterials

3.1 Introduction

Ionic self-complementary oligopeptide biomaterials are a novel class of biomaterials that represents great potential for applicability in tissue engineering. They possess many properties that make them ideal candidates for use in the area of tissue reconstruction. This class of biomaterials consists of small peptides that self-assemble into a stable macroscopic matrix when exposed to a salt solution. The matrix is resorbable and degrades into natural amino acids. As a result, their use as a biodegradable polymeric material would obviate toxicity problems and side effects associated with the degradation of other biomaterials. These oligopeptide based biomaterials could be used for applications as scaffolds to support cell adhesion, wound dressings, bioadhesives, and other medical devices. This chapter discusses the properties of the ionic self-complementary oligopeptides and how these can be of benefit in tissue engineering applications.

3.2 Ionic Self-Complementary Oligopeptides

3.2.1 Background

Ionic self-complementary oligopeptide biomaterials have been recently developed by Dr. Zhang in the Department of Biology at Massachusetts Institute of Technology, Cambridge, Massachusetts (1, 2, 3). They consist of a family of oligopeptides with alternating hydrophobic and hydrophilic proteogenic amino acids. The amphiphilic nature of the peptides is such that they are soluble in water. The hydrophilic residues are in alternating +/- charge groups, complementing each other's charge and resulting in neutrally charged peptides. The oligopeptides form unusually stable β -sheets in water (1, 2). The peptide solutions spontaneously self-assemble into a macroscopic membrane when exposed to monovalent salts, producing a hydrated matrix that is insoluble and physically stable.

The first oligopeptide in the mentioned class of biomaterials to be developed was EAK16. The letters E, A, and K represent the component amino acid residues glutamate, alanine, and lysine, respectively. The structures of these three amino acids is shown in Figure 3.1.

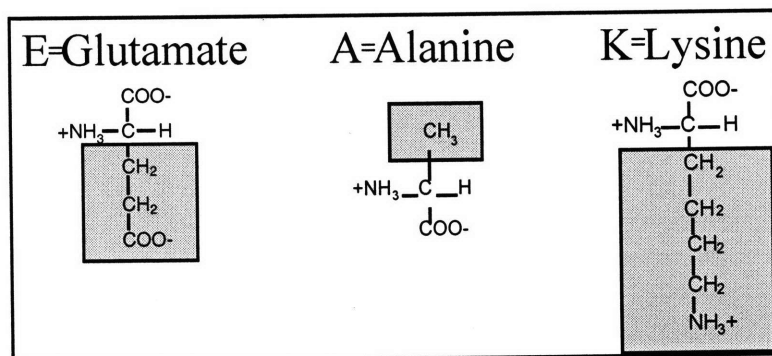


Figure 3.1. Amino acid components of EAK oligopeptides. Shaded part includes the characteristic residue.

The number following the amino acids, namely 16, indicates the number of amino acids in the peptide. The specific sequence for EAK 16 is (N-AEAEAKAKAEAEAKAK-C), where C- and -N are the C, or carboxylic, and N, or amino, terminus, respectively. In the sequence, A is the aliphatic component while E and K, are the ionic hydrophilic components. E and K have respective pKa values of 4.3 and 10.5 (5), resulting in respective negative and positive charges at neutral pH.

As the other peptides in the class of biomaterials under discussion, EAK16 shows a stable β -sheet conformation in water (1). This stable structure is unusual for such small peptides. Unlike proteins, which in general have well-defined three-dimensional structures, peptides usually have structures with considerable freedom of movement and lack tertiary structures (4). When exposed to monovalent salt, the peptide forms a macroscopic membrane consisting of an interwoven mesh of filaments, as seen by scanning electron microscopy (1). The filaments have diameters of 10 to 20 nm and are separated by distances of 50 to 80 nm (1).

The self-assembly of EAK16 and all other ionic self-complementary oligopeptides is due to collective weak interactions which are non-covalent intermolecular interactions between different peptide chains. These weak interactions, which consist of hydrogen bonds and charged ionic, hydrophobic, and van der Waals interactions, provide the organizational drive for the oligopeptides' self-assembly. In the

β -strand conformation, the peptide backbone is fully extended forming a zigzag or pleated chain (5). The peptide bond between adjacent amino acids is planar and the resulting pleated chain is nearly co-planar (5, 6). The residues of adjacent amino acids are "sticking-out" on alternating sides of the zigzag chain (5). In self-complementary peptides, since the amino acid sequence alternates hydrophobic and hydrophilic residues, all the hydrophobic and the hydrophilic groups lie on opposite sides of the backbone. This spatial segregation of side groups based on hydrophobicity allows each side of a peptide molecule to come into proximity with a matching-hydrophobicity side on a second peptide. Non-polar residues come close together to repel the aqueous solvent, water in most cases, and form apolar or hydrophobic bonds (7). The polar or hydrophilic groups are attracted to each other by the electrostatic effect resulting from their opposite, or complementary, charges (7). Thus, the amino acid residues give the oligopeptide sides a specificity to attract each other as a biological "zipper." A schematic of these interactions is shown in Figure 3.2a, 3.2b, and 3.2c. Figure 3.2a depicts a single peptide fragment. The opposite directions of the groups can be observed with hydrophobic groups directed into the page and polar groups directed out of the page. Part b of the figure shows the hydrophobic interaction bringing the apolar groups into proximity. The electrostatic attraction of complementary charges is sketched in part c.

Additional non-covalent interactions are provided by hydrogen bonds and Van der Waals forces. The hydrogen bond, ionic in nature, consists of the attraction of an electronegative atom such as nitrogen or oxygen to a hydrogen atom covalently linked to another electronegative atom (7). This type of bond can be formed by numerous groups in biomolecules. In peptides, these groups include the nitrogen and oxygen in peptide bonds and the amino and carboxyl groups of charged residues (7). Of special importance is the hydrogen bond between the peptide linkage oxygen and nitrogen of separate peptides in β -sheet conformation. The "zigzag" shaped β -sheet backbones are linked together forming a "zigzag" shaped sheet known as the β -Pleated sheet. A schematic of this structure is shown in Figure 3.2 d. A final contribution is made by Van der Waals forces, which result in attraction between any two atoms in close proximity.

Compared to covalent bonds, non-covalent interactions form rather weak bonds. Non-covalent bonds have dissociation energies ranging from approximately 1 to 20 kJ/mol. The energies from these weak interactions are several orders of magnitude lower than covalent bonds. Typical covalent bond energies are 248 and 611 kJ/mol for single and double carbon-carbon bonds (7). However, the sum of the numerous weak interactions gives the stability to the structures and aggregates of many biomolecules.

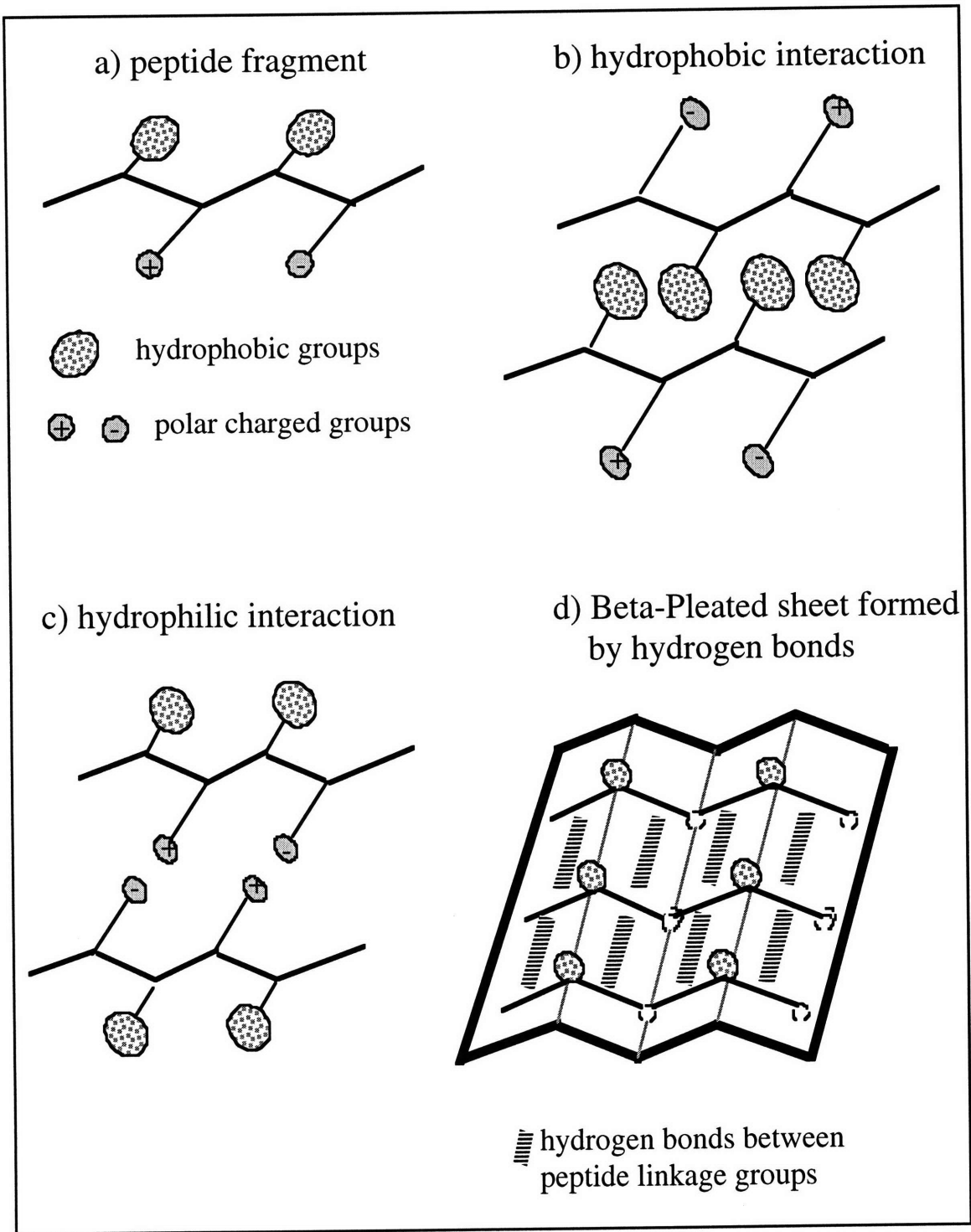
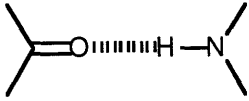

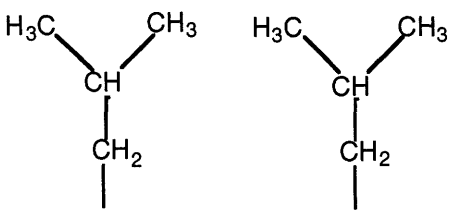
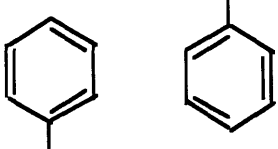

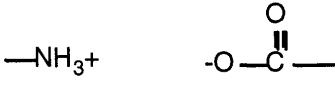


Figure 3.2 Schematic of weak interactions in peptides.

Table 3.1 Non-Covalent Interactions in Biomolecules*

Weak Interaction		Stabilization Energy (kJ/mol)
Hydrogen Bonds - peptide bonds		8 - 21
Hydrophobic Interactions - alanine residue		1
- leucine residue		6
-stacking of aromatic rings		6
Ionic Interactions -repulsion		-21
- attraction		42
Van de Waals	attraction between any two atoms in proximity	4

* Adapted from references 5 and 7.

In the case of ionic self-complementary biomaterials, weak interactions result in the formation and stability of a macroscopic self-assembled matrix. A list of some of these weak interactions and their respective stabilization energies is included in Table 3.1 (5, 7).

The precise mechanisms involved in the oligopeptide self-assembly are not yet completely understood. A model based on the knowledge weak interactions in β -sheet peptides has been proposed (1, 2). This model states that the oligopeptide monomers form β -Pleated sheets with interchain hydrogen bonds. The pleated sheets could be of the parallel or antiparallel form (1). Since the monomers could be staggered, the pleated sheet could extend indefinitely in the 2-D plane they form. As discussed earlier, the polar and apolar residues would lie in opposite sides of the monomer backbone. As a result, one side of the 2-D sheet has hydrophobic groups protruding from it, while the opposite side has hydrophilic groups. Therefore, the intermolecular hydrophobic and hydrophilic interactions discussed earlier and shown in Figure 3.2 occur between the polymeric sheets rather than between single monomers. A schematic of the proposed assembly model is shown in Figure 3.3. The model shows that the β -sheets, formed by intermolecular hydrogen bonding, stack alternating hydrophobic and hydrophilic sides. That stacking provides the third dimension in the matrix assembly. This assembly results in the formation of filaments or fibers. These filaments are self-interwoven and form a macroscopic mesh or porous matrix.

3.2.2 Amino acid Composition of Oligopeptides

The ability of self-complementary oligopeptides to self-assemble depends on its amino acid composition. Peptides can be synthesized with any number and sequence of amino acids. Both of these parameters, namely number of residues and specific sequence, will affect the peptide's properties significantly. This fact has to be taken into account when designing a new self-complementary oligopeptide.

As stated earlier, EAK16 (Ac-HN-AEAEAKAKAEAEAKAK-CONH₂) was the first member of the class of biomaterials under discussion to be developed. It has β -sheet conformation in water and associates to form a macroscopic matrix (1). The 16-mer was shortened by removing 4 and 8 amino acids resulting in EAK12 (Ac-HN-AEAKAEAEAKAK-CONH₂) and EAK8 (AcHN-AEAEAKAK-CONH₂), respectively. The AcHN- and -CONH₂ indicate that the N terminus is acetylated and the C terminus is aminated. This prevents the N and C termini from being protonated and deprotonated,

respectively. The capping of the termini showed no effect on the self-assembly process (1). EAK12 showed β -sheet conformation as well as α -helix conformation in water. As a result, EAK12 associated to a smaller extent (1). On the other hand, EAK8 did not form β -sheets and was simply a random coil, which indicates the absence of a particular conformation (1). EAK8 did not self-assemble (1). Similar results were observed with the oligopeptide sequence RAD. RAD16(AcHN-RARADADARARADADA-CONH₂) forms β -sheets and self-assembles while a shorter sequence, RAD8, results in random coils and does not self-assemble (2). These short peptides cannot form overlapping staggering due to the very weak alanine-alanine interactions. These data show that the length of the peptide has a significant effect in inducing β -sheet formation and ability to self-assemble.

The amino acids in the peptide sequence also play an important factor in inducing β -sheet conformation and self-assembly. As mentioned above, EAK8 did not form β -sheets and did not self-assemble (1). However, replacing the hydrophobic alanine, A, by phenylalanine, F, results in a self-associating material. Phenylalanine is an aromatic hydrophobic group. Its structure is shown in Figure 3.4 *a*. As other aromatic amino acids, phenylalanine provides a very “bulky” R group. Its R group is much more hydrophobic than alanine’s CH₃. This can be seen by comparing their hydrophobicity index. The hydrophobicity index is a scale of hydrophobicity-hydrophilicity that predicts whether an amino acid will be found in aqueous (- value) or in hydrophobic environments (+ values) (5). The index value for phenylalanine is 2.8 while that for alanine is 1.8 (5). As seen in Table 3.1, hydrophobic interactions of the alanine R group have a stabilization energy of only 1 kJ/mol. This value is much smaller than that for the stacking of aromatic rings, namely 6 kJ/mol. Phenylalanine has the stacking potential in addition to an extra contribution from the CH₂, which makes it more hydrophobic. Therefore, phenylalanine provides stronger hydrophobic interactions in peptides than alanine. The combined effect of these properties of phenylalanine can give an 8-mer the tendency to form β -sheets and self-assemble. The substitution of the A’s of EAK8 by F’s, gives a peptide of β -conformation that self-assembles, namely EFK8 (N-FKEFKFEF-C). The chemical structures of EFK8 and its R groups are included in Figure 3.4

Replacement of one of the amino acid constituents in a peptide has a great effect on the peptide’s properties. Replacing of the A on a EAK8, a peptide that does not

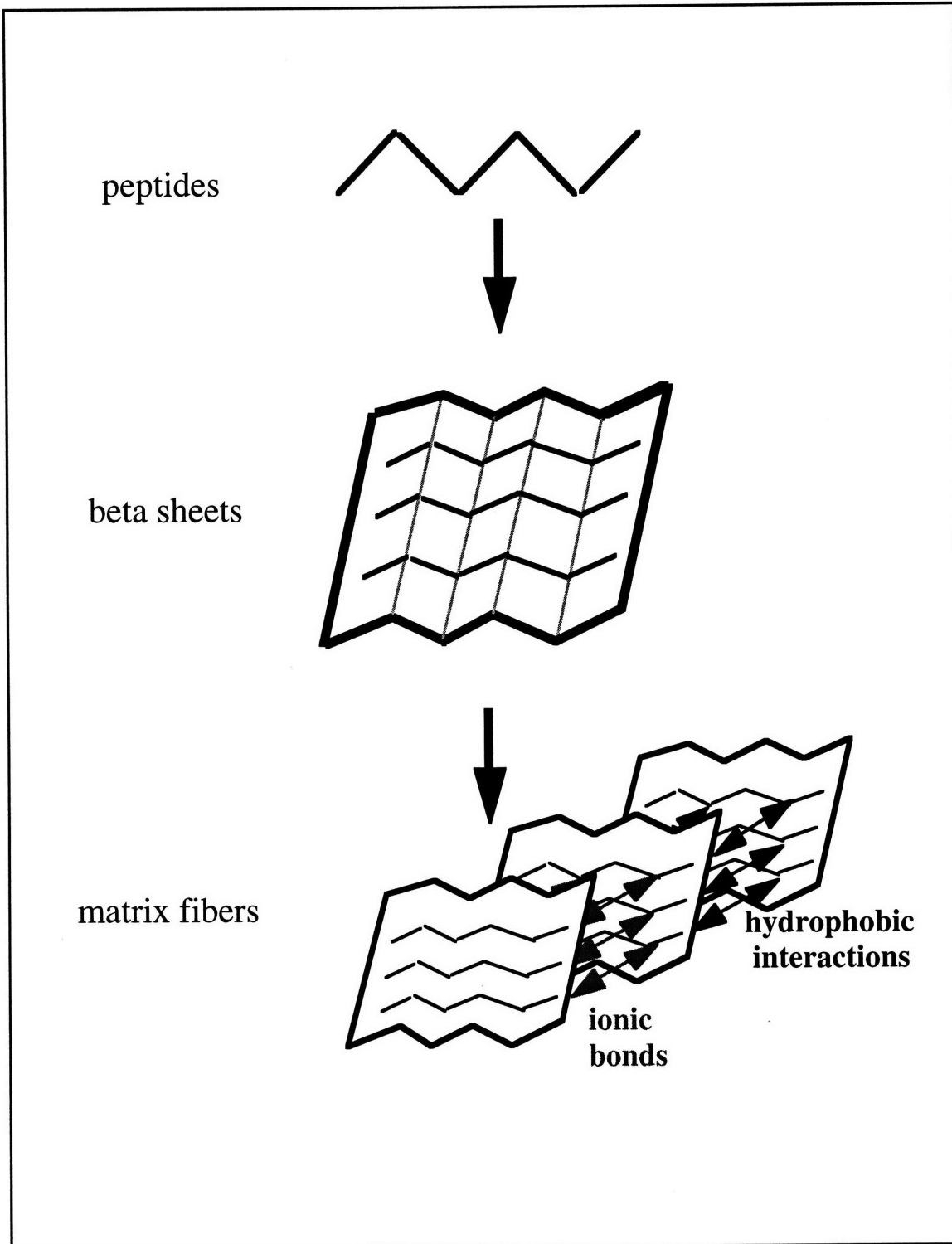


Figure 3.3 Proposed model for peptide assembly

assemble, by F resulted in EFK8, a peptide that self-assembles. However the higher hydrophobicity of F makes EFK8 much more hydrophobic than EAK8. As a result, EFK8 will be soluble in water to a much smaller extent than EAK8. The EAK sequence can be extended to form the 16-mer EAK16. EAK 16 is soluble in water and self-assembles. Its maximum solubility in water is approximately 5 mg/ml. On the other hand, extending the EFK sequence into a 16-mer, namely EFK16, results in a peptide that is extremely hydrophobic and will not dissolve in water. Therefore, an increase in hydrophobic interactions results in a decrease in peptide solubility. This fact presents a trade-off that must be considered when designing oligopeptide biomaterials.

The peptides poly(EF) and poly(KY), where Y represents tyrosine, have been reported not to self-assemble into macroscopic structures (Zhang 1996). Poly(EF) and poly(KY) are sequences of repeating EF and KY patterns respectively. Furthermore, the peptides of (RF)₁₀ and (VE)₁₀, consisting of 5 repetitions of RF and VE, respectively, did not show apparent self-assembly property (Zhang 1996). These peptides do not assemble in spite of the large hydrophobicity of F, Y, and V, or valine. These observations suggest that both positive and negative charges are important to facilitate peptide self-assembly.

3.2.3 Properties

Ionic-self-complementary oligopeptide biomaterials possess numerous properties that make them attractive for biomedical applications. They are composed of natural amino acids, which are normally found in human metabolic processes. Using them dissolved in water will not present harmful effects to humans. Some of the peptides that are insoluble in water may self-assemble in solutions with organic solvents. However, for biological applications solubility in water is more attractive than solubility in organic solvents. It is these water soluble self-associating peptides, such as EFK8 and EAK16, that present great potential for medical applicability.

The oligopeptides and assembled matrices show great physical and chemical stability. EAK16 showed a stable β -sheet structure at temperatures ranging from 25 to 90°C (2). It also showed stability at pH levels ranging from 1 to 11 (2). Furthermore, the structure of EAK16 was not significantly affected by denaturing agents including 7M guanidine-HCl and 8M urea. Denaturing agents usually cause a total loss or randomization of the three-dimensional structure by disrupting the weak interactions or altering charges (5). Similar stability was observed for RAD16. The assembled matrices of EAK16 and RAD16 also show thermal and chemical stability (3). The heat and

chemical stability give the peptides resistance to adverse disturbances that might otherwise impede their function as medical biomaterials.

The oligopeptide biomaterials exhibit a biological compatibility ideal for medical applications. Matrices of EAK16 and RAD16 support attachment of mammalian cells (3). Cells including mouse fibroblast, hamster pancreas, human foreskin fibroblast, and human epidermal keratinocytes attached to both oligopeptide matrices for over 2 weeks (3). Also, both materials did not elicit immunologic response when injected into rabbits alone and conjugated with other proteins (3). These properties of cell attachment and lack of immunogenicity can be of benefit for tissue engineering applicability.

Furthermore, the material is easily processable. As mentioned earlier, the peptides self-assemble when exposed to monovalent salts. Therefore injection of peptide solution into a tank filled with salt solution will promote association of the peptides. If injection rates allow the diffusion of salt into the injected peptide, the peptide will assemble into a matrix with the geometry of the extruded peptide. That is, the resulting matrix will have the shape of the injection device. Matrices shaped as cylinders and rectangular tapes have been fabricated this way. Matrices could also be shaped by filling a mold with peptide and submerging it into a tank of saline. The use of extrusion, molding, or other processing techniques could allow the fabrication of macro-pores that might be required for applications such as cell scaffolds. Moreover, the material could be shaped in situ. Since it assembles in physiological conditions, it can be applied as a liquid solution. This capability would ease the filling of small gaps eliminating the problems of shaping solid implants into complex geometries.

3.3 EFK8

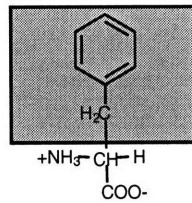
This study concentrates on EFK8 (N-KFEFKFEF-C). Its chemical structure and that of its components are shown in figure 3.4. As in EAK16, the negative and positive polar amino acids are glutamate, E, and lysine, K, respectively. The hydrophobic R-group is provided by the aromatic amino acid phenylalanine, F. A molecular model of EFK8, performed with Molecules 3-D, is included in Figure 3.5. This model clearly shows the bulky hydrophobic phenylalanine R groups lying on one side of the β -sheet and the charged glutamate and lysine R groups lying on the opposite side.

EFK8 is one of the smallest peptides in the family of self-complementary oligopeptide biomaterials. Presently, 8-mers are the smallest peptides that form part of this class of materials. Previous studies suggest that longer peptides are more stable than shorter ones and show greater tendency to self-assemble. However, the shortest peptides

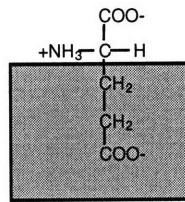
present the advantage of lower cost and greater ease of synthesis. Also, shorter peptides show lesser structural and chemical complexity, which facilitate their study. Therefore, the study of small peptides provides the starting point in the path towards greater comprehension of the oligopeptide biomaterials.

a)

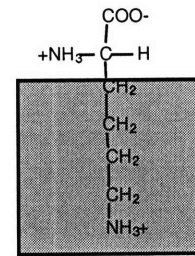
F
Phenylalanine
(hydrophobic)



E
Glutamate
(polar negative)



K
Lysine
(polar positive)



b) C-FEFKFEFK-N

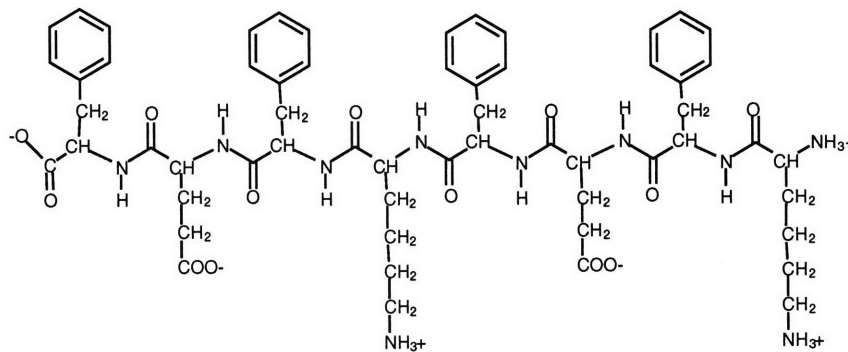


Figure 3.4 Chemical structure of EFK8: a) component aminoacids with R groups shaded and b) peptide.

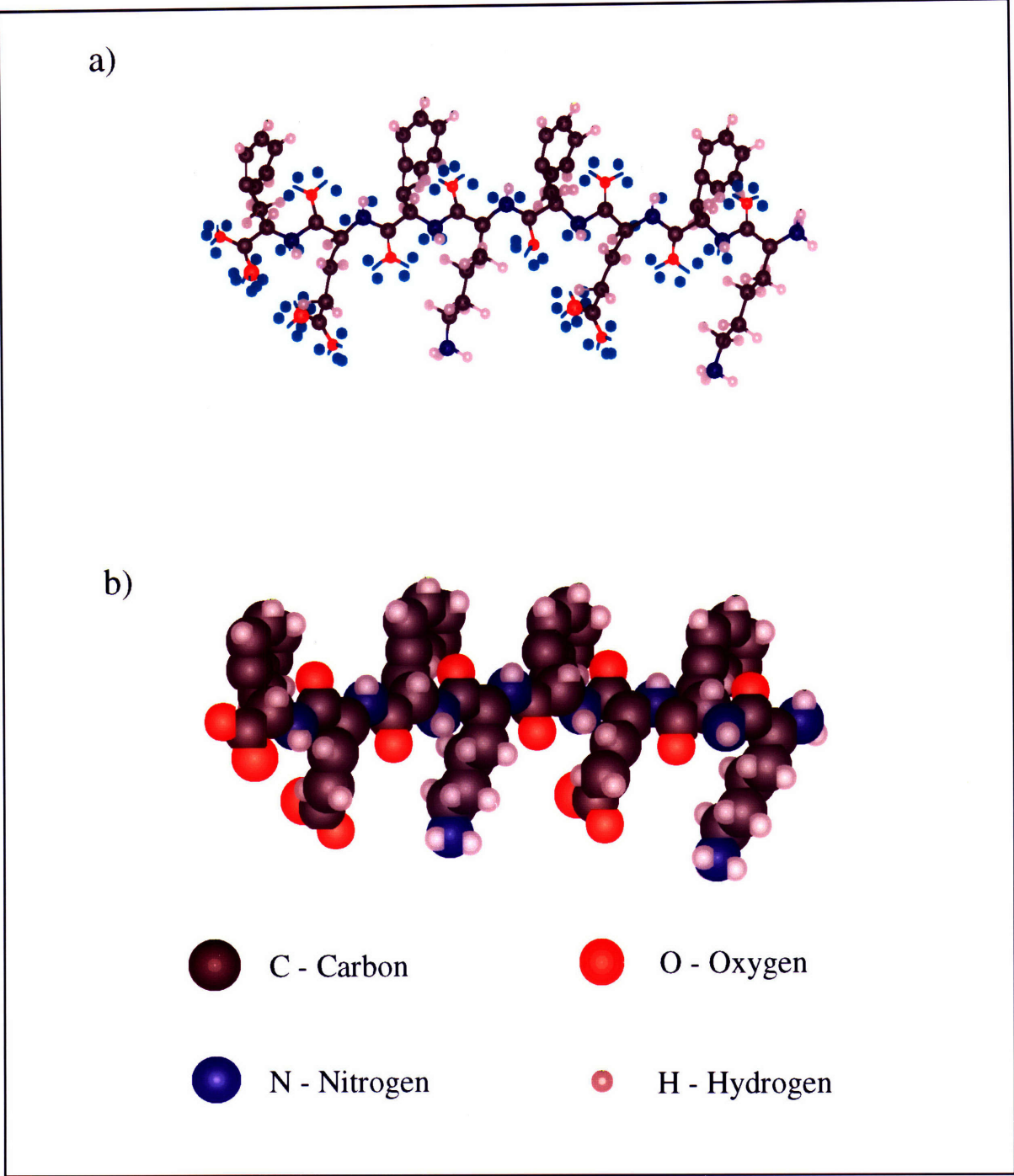


Figure 3.5 Molecular model of EFK8: a) ball and stick view and b) space-fill model.

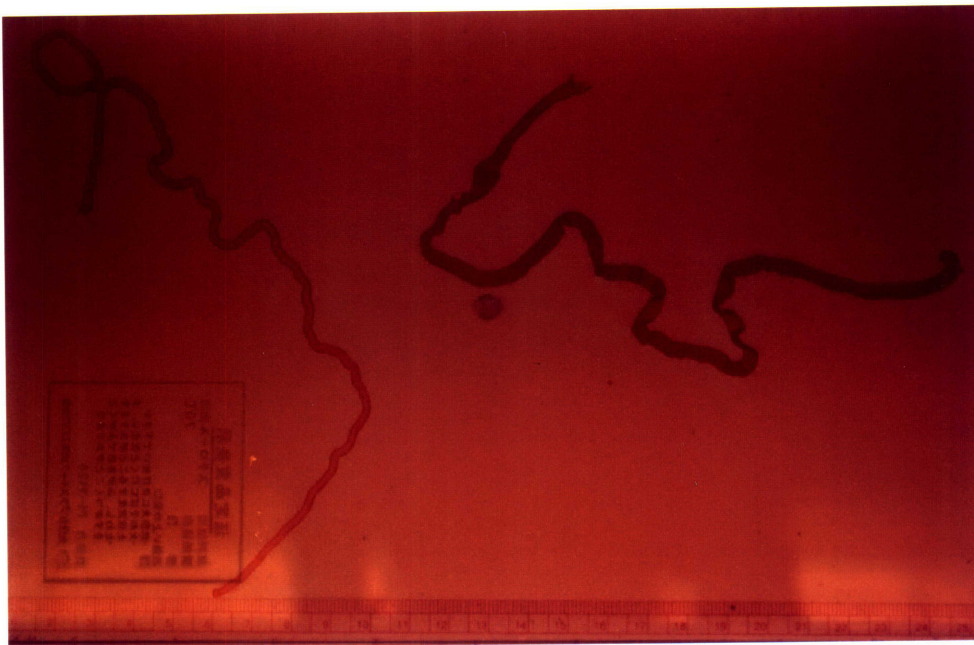
3.4 References

1. Zhang, S., T. Holmes, C. Lockshin, and A. Rich. "Spontaneous Assembly of a Self-Complementary Oligopeptide to Form a Stable Macroscopic Membrane," *Proceedings From the National Academy of Science USA*, Vol. 90, pp. 3332-3338, 1993.
2. Zhang, S., C. Lockshin, R. Cook, and A. Rich. "Unusually Stable Beta-Sheet Formation in an Ionic Self-Complementary Oligopeptide," *Biopolymers*, Vol. 34, pp. 663-672, 1994.
3. Zhang, S., T.C. Holmes, C.M. DiPersio, R.O. Hynes, X. Su, and A. Rich Self-Complementary Oligopeptide Matrices Support Mammalian Cell Growth," *Biomaterials*, Vol. 16, pp. 1385-1393, 1995.
4. Bailey, P. D. *An Introduction to Peptide Chemistry*, New York: Arau, pp. 1-41 and 182-202, 1990.
5. Lehninger A. L., D. L. Nelson, and M. Cox. *Principles of Biochemistry*, New York: Worth Publishers, pp. 160-193, 1993.
6. Bodansky, M. *Peptide Chemistry, 2nd ed*, New York: Springer-Verlag, pp. 39-52, 1993.
7. Frieden, E. "Non-Covalent Interactions: Key to Biological Flexibility and Specificity," *Journal of Chemical Education*, Vol. 52, pp. 754-761, 1975.

Appendix 3.A

Picture of Macroscopic Oligopeptide Matrices

The tapes of oligopeptide material shown below were fabricated with a rectangular injection device. The resulting colorless tapes were stained with congo red. The scaling on the bottom indicates centimeters.



Courtesy of S. Zhang, MIT Biology Department

Chapter 4

Structural Analysis with Scanning Electron Microscopy

4.1 Introduction

Scanning electron micrographs of the oligopeptide materials were analysed to gain insight about their matrix structure. The electron microscopy is frequently used to determine the regularity and isotropy, or lack thereof, of polymeric structures. The micrographic analysis allowed the identification of some key structural features of the matrix such as the fibers' thickness and the distance between them. The structural information could be useful in better understanding the self-assembly process involved in the peptide polymerization. Moreover, knowledge of the matrix structure provides assessment of some of the differences between the various oligopeptide materials. These structural differences could clarify the difference in mechanical properties between various members of the oligopeptide materials family.

4.2 Specimen Preparation

Preparation of specimens for the Scanning Electron Microscope (SEM) involves various steps. Since the SEM operates on a high vacuum, samples must be fixed and dehydrated before scanning. Fixation is usually done with an aldehyde that introduces inter- and intra-molecular crosslinks. The sample is then dehydrated and later dried with methods such as air-drying and critical-point drying. Moreover, non-conducting samples require application of a thin coat of conducting metal. If not coated, the surface of a non-conducting specimen will become charged, impeding the acquisition of SEM images (1).

Peptide matrix samples of EFK8 at 3.3 and 10 mg/ml, RADA16 at 2 mg/ml, and RFE8 at 12 mg/ml were prepared for observation with the SEM. The matrices were fabricated by pipetting 0.15 ml of peptide solution into 0.1M phosphate buffered saline (PBS). The contents of PBS are listed in the Materials section in Appendix 4.A. The matrices were left immersed in PBS for 25 minutes to allow total gelation of the peptide. The samples were then prepared for SEM following the protocol included in Appendix

4.A, which is summarized below. The samples were fixed with glutaraldehyde at 4°C for 2 hours. The fixed matrices were then dehydrated by immersing in graded solutions of ethanol in PBS. The ethanol concentration was increased from 0 to 100% to remove all the water in the matrix. The samples were then dried by CO₂ critical-point drying. An alternative to critical-point drying consisting of sample immersion in Hexamethyldisilazane (HMDS) followed by air drying was tried for EFK8 at 3.3 mg/ml and RADA16 at 2 mg/ml. The HMDS is used to prevent the collapse experienced by biological materials when air dried. HMDS followed by air drying has given comparable results to critical-point drying for SEM studies of polyethylene oxide hydrogels, insect tissues, and mammalian tissues (2, 3, 4). Since the matrix is non-conducting, it was coated with gold-palladium using a sputter coater.

4.3 SEM

4.3.1 SEM Imaging

The samples were observed using a JEOL JSM-6320FV field emission SEM. Photographs were taken at various magnifications ranging from x2,000 to x100,000. The SEM micrographs are included in Figure 4.1 - 4.4. Figure 4.1 includes the micrographs of EFK8 at 3.3 mg/ml. RADA16 at 2 mg/ml is depicted in Figure 4.2. Figure 4.3 corresponds to EFK8 at 10 mg/ml. Pictures of RFE8 at 12 mg/ml are shown in Figure 4.4.

4.3.2 Results

The micrographs obtained from critical-point dried samples of EFK8, RADA16 and RFE8 are included in Figure 4.1 - 4.4. As seen in these figures, the macroscopic membrane formed by the peptides consists of a low density fibrous material with structure resembling that of cotton wool. At the lower magnifications, namely x2000 and x4000, the specimen has the appearance of a continuous solid with a rough surface. At the higher magnifications of x16000 and x32000 the materials' porous structures becomes discernible.

The materials can be described as a mesh of randomly interconnected fibers. This cellular network is similar to the one observed for another ionic self-complementary oligopeptide, EAK16 (6). This fibrous structure suggested a proposed model for the formation of the macroscopic matrix, as described in Chapter 3. In this model, the peptides assemble in a staggered fashion and aggregate into filaments (6). These filaments are interwoven forming a macroscopic porous matrix (6). The micrographs for

all the specimens suggest that the fibers are randomly oriented. The fibers do not show any palpable preferred orientation. No obvious variations with direction in fiber thickness or edge-connectivity distances are observed in the pictures. The matrices, however, exhibit some irregularities.

The structures of EFK8 at 3.3 mg/ml and RADA16 at 2 mg/ml are indistinguishable. Their fibrous networks have a fairly uniform appearance. Both peptides resulted in matrices with estimated fiber thickness of 10 to 30 nm and distance between fibers of 100 to 250 nm. The high magnification micrographs of EFK8 at 10 mg/ml differ significantly from those of the same peptide at 3.3 mg/ml. Comparison of their respective pictures distinctly illustrate that the 10 mg/ml peptide dilution resulted in a denser matrix. The fibers have similar thickness, however, the 10 mg/ml sample has a larger number of fibers per volume. Their interwoven fibers crossing junctions are separated by shorter distances, resulting in shorter mean fiber length. This length is approximately 50 to 100 nm. Besides, the network of the 10 mg/ml sample is less uniform than that observed at 3.3 mg/ml. The structure of the 10 mg/ml specimen has solid clumps of peptide material. These lumps are clearly seen in the respective x65000 and x100,000 respective magnifications of Figure 4.3e and 4.3f, respectively. RFE8 at 12 mg/ml shows a structure very distinct from those of EFK8 and RADA16. As seen in Figure 4.4, this material has thicker fibers than the other peptide materials. These fibers have roughly estimated diameters of 80 to 120 nm, or about three times those for EFK8 and RADA16. Like EFK8 at 10 mg/ml, RFE8 exhibits a denser fibrous structure denser than either RADA16 at 2 mg/ml or EFK8 at 3.3 mg/ml. RFE8 also shows certain non-uniformities in structure. These variations are not as obvious as the lumps in EFK8 at 10 mg/ml, but are noticeable when the micrographs at magnifications of x40000, x65000, and x100000 in Figure 4.4 are compared. The x40000 magnification in Figure 4.4d seems less dense than x65000 and x100000 in Figure 4.4e and Figure 4.4f, respectively. The fibers in the x40000 figure show approximate length between junctions of 400 to 1000 nm. The higher magnifications have fibers of lengths in the order of 100 to 300 nm. These variations in structure within an RFE8 specimen could be the result of material clumping in certain areas of the matrix.

The specimens prepared by HMDS with air drying collapsed. These specimens shrank significantly. After air-drying, they had a solid appearance instead of the fibrous, cotton-like foamy appearance showed by the critical-point dried samples. In the SEM, the specimens showed a rugged solid surface. The fiber-network and pores could not be observed due to the structural collapse.

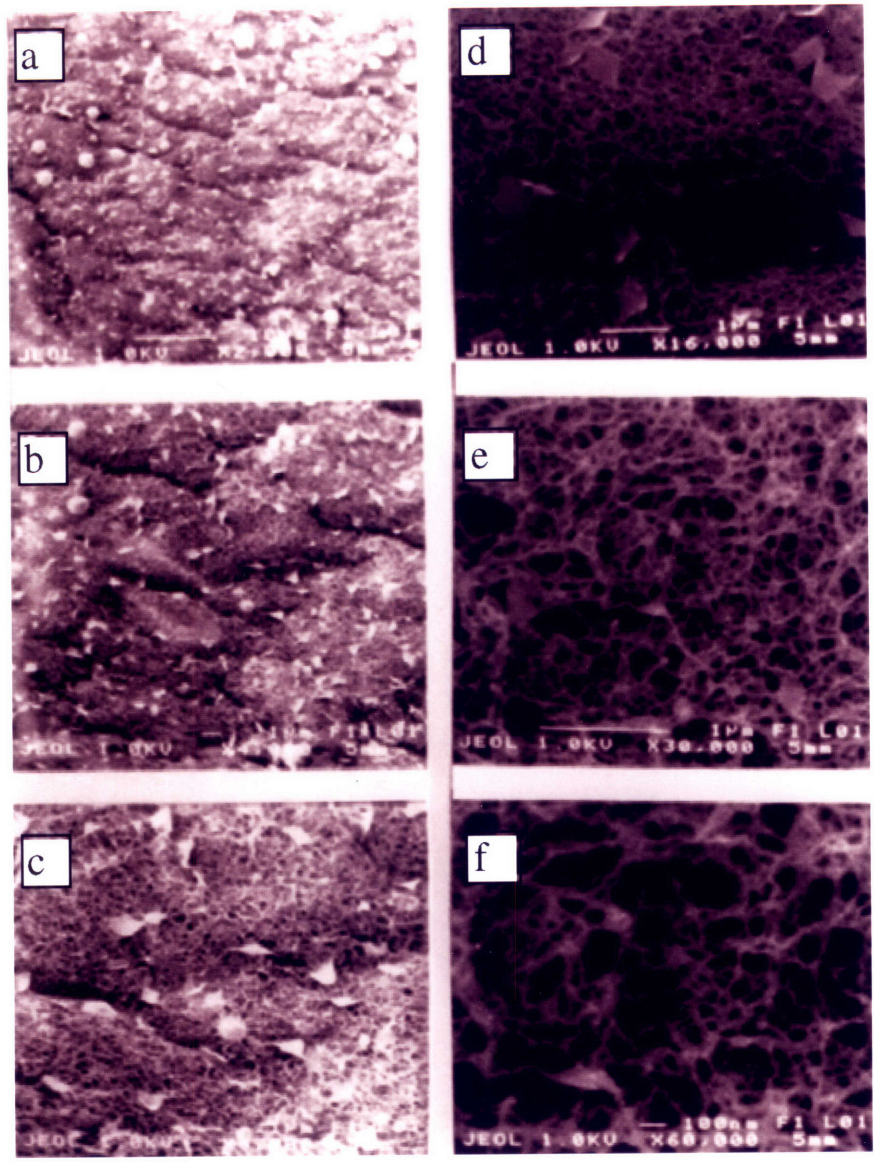


Figure 4.1. SEM's of EFK8 at a concentration of 3.3 mg/ml. Magnifications of a) x2,000, b)x4,000, c)x8,000, d)x16,000, e)x32,000, and f)x60,000.

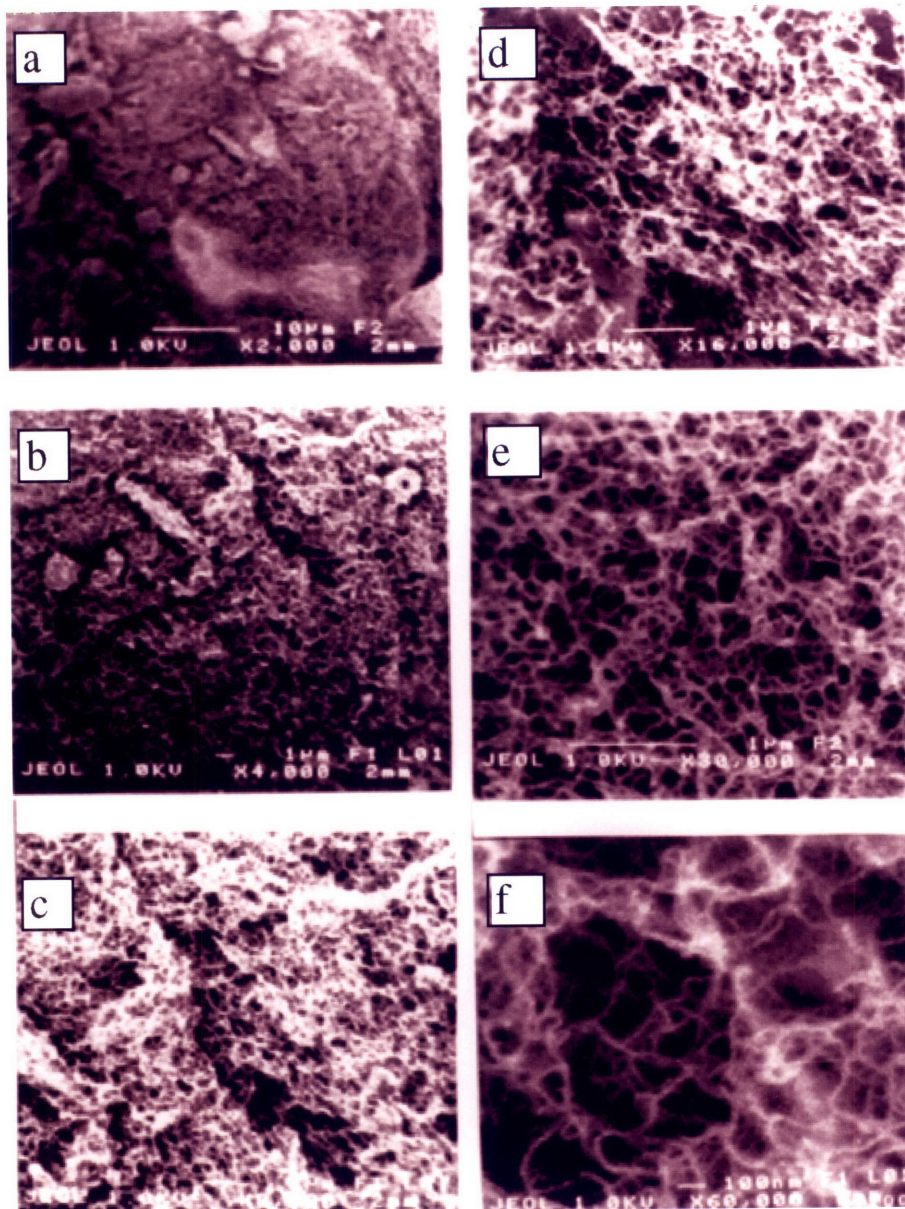


Figure 4.2. SEM's of RADA16 at a concentration of 2 mg/ml. Magnifications of a)x2,000, b)x4,000, c)x8,000, d)x16,000, e)x30,000 and f)x60,000.

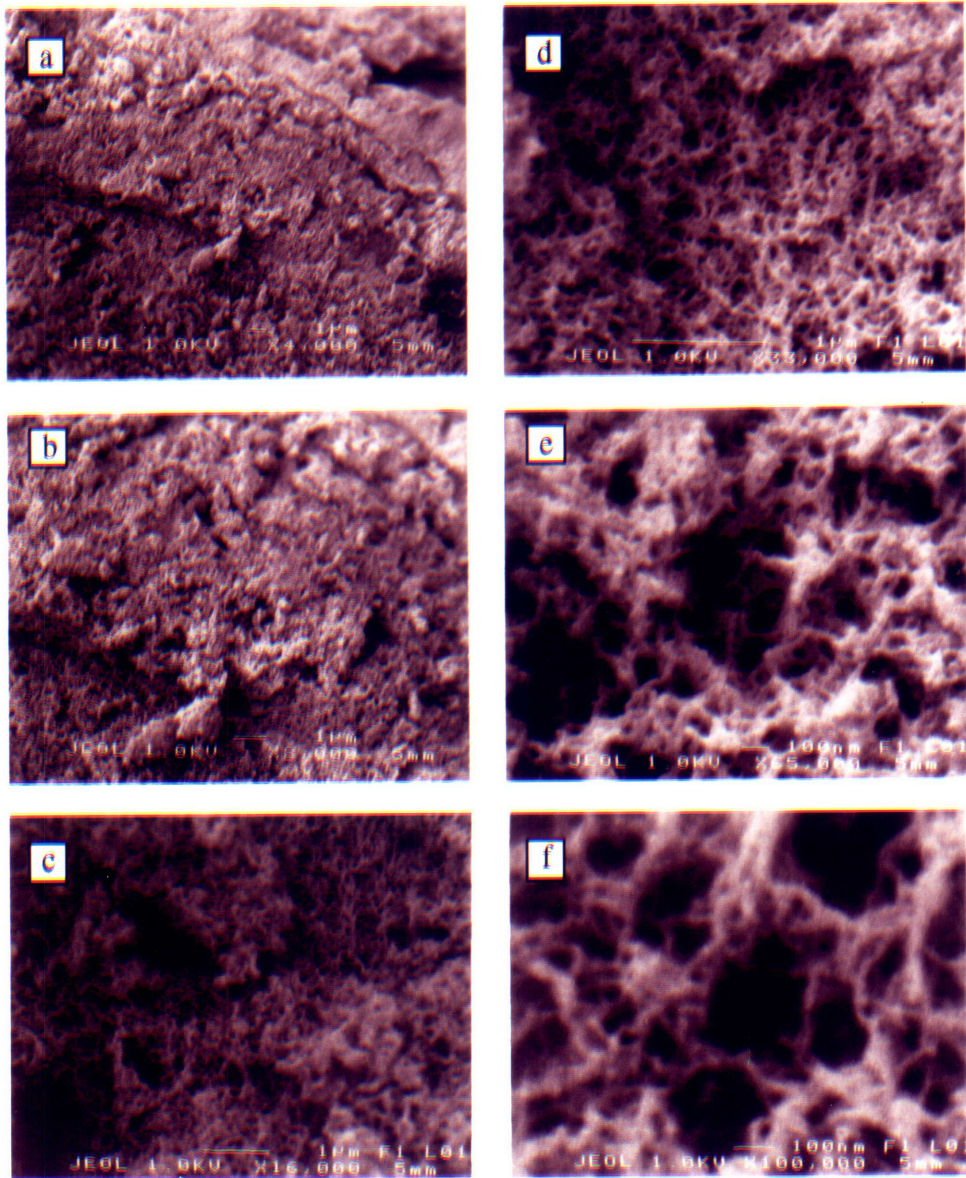


Figure 4.3. SEM's of EFK8 at a concentration of 10 mg/ml. Magnifications of a)x4,000, b)x8,000, c)x16,000, d)x33,000 e)x65,000, and f)x100,000

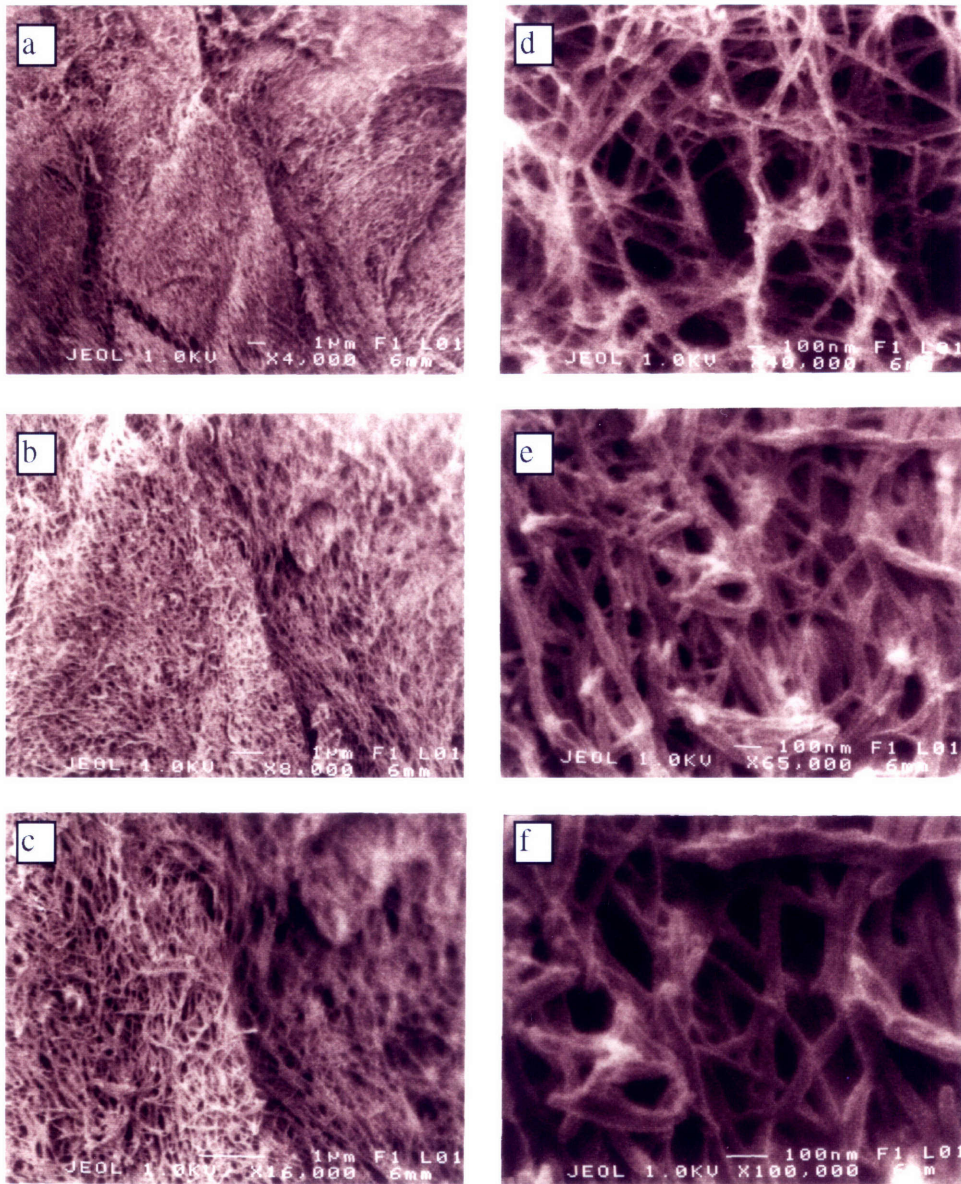


Figure 4.4. SEM's of RFE8 specimen. Magnifications of a)x4,000, b)x8,000, c)x16,000, d)x40,000, e)x65,000, and f)x100,000.

4.3.3 Image Analysis

Image analysis was performed on scanning electron micrographs of EFK8 to quantify the structural parameters relevant to mechanical properties. The analysis was performed on a Macintosh 8500 Power PC using the public domain NIH Image program. The micrographs used for the analysis were taken from samples of EFK8 at 3.3 and 10 mg/ml at a magnification of x100,000.

To characterize the structure of the cellular material it is necessary to determine the thickness of the fibers and the distance between them, or edge length, l . Using the NIH software, the length and area of the fibers in the micrograph were measured. The fiber length measured from the 2D image is the length projected on the image plane. This projected length will depend on a fiber's orientation in space. Therefore, a correction for orientation needs to be made when calculating the average fiber length.

The average projected length \bar{l} is the average of the lengths measured on the SEM. It is given by

$$\bar{l} = \frac{1}{N} \sum_{i=1}^N l_i \quad (4-1)$$

where N is total number of fibers and l_i is the measure projected length of the i^{th} fiber. Assuming that the fibers are randomly oriented in space, the characteristic length is given by

$$l = \bar{l} \frac{4}{\pi} \quad (4-2)$$

The derivation of equation 4-2 is detailed in Appendix 4.B. The thickness of each fiber was calculated by dividing its area A_i by its projected length l_i . The characteristic thickness was taken to be the average of the calculated fibers' thickness and is given by

$$t = \frac{1}{N} \sum_{i=1}^N t_i = \frac{1}{N} \sum_{i=1}^N \frac{l_i}{A_i} \quad (4-3).$$

These data can be used to calculate the relative density of the material. The relative density is simply the ratio of the matrix density ρ^* to the density of the solid fibers ρ_s .

Therefore, it represents the solid fractional volume of the matrix. This ratio depends on the geometry of the matrix structure. From geometrical considerations, the relative density can be written in terms of t and l as

$$\frac{\rho^*}{\rho_s} = C_1 \left(\frac{t}{l} \right)^2 \quad (7). \quad (4-4)$$

This equation is valid for open-cell foams with low relative density, or $t \ll l$ (7). The numerical constant C_l in equation 4-4 is close to unity and depends on the geometry of the cellular aggregates formed by the connected fibers. For a square prism with aspect ratio A_r , C_l is given by

$$C_l = \left(1 + \frac{2}{A_r} \right) \quad (4-5)$$

(7). So a square-prism cell with aspect ratio of 1 results in C_l equal to 3. Higher aspect ratios lead to smaller values. Polyhedral cells given by triangular and hexagonal prisms have respective C_l values of 4.6 and 1.9.

The measurements of the desired parameters from micrographs present some difficulties. Since the matrix is a three-dimensional structure, the observed 2-D image depicts overlapped projections of fibers at different depth levels within the matrix. As a result, crossing of fibers at different planes depths might look like edge-connections. This complicates the identification of true junctions in the matrix. Therefore, discerning between true junctions and fiber overlaps requires the experimenter's judgment. One must establish which fiber crossings do not represent junctions by careful examination of original high quality prints of the images. In these prints the illumination and shades assist in determining the depth levels of fibers. This information can often identify crossings that are not true junctions. This idea is illustrated in Figure 4.5b. This figure shows 7 fibers marked in a duplicate of the micrograph in Figure 4.5a. This micrograph corresponds to EFK8 at 3.3 mg/ml and x100000 magnification. The fiber marks are numbered 1 through 7. Fibers 1 through 4, delineated by gray lines with arrowheads, are fibers lying at the surface. These fibers are incorporated in the measurements. Fibers 5 through 7, delineated by white lines without arrowheads, exhibit overlap shades that indicate their location at depths below the surface. Consequently, these fibers are neglected in the measurements. Neglecting fiber 5 signifies that there is no node connecting fibers 1, 2 and 5. Thus, fibers 1 and 2 are actually a single fiber or edge and are measured as such. Similarly, fibers 3 and 4 represent a single fiber giving a single length measurement. If these fibers were included, edge length measurements would be underestimated. This has the effect of overestimating the relative density .

The analysis of the EFK8 images assumes that the fibers form square prisms with aspect ratio of 1. The micrograph used for the analysis of EFK8 at 3.3 mg/ml is shown in Figure 4.5. A total of 81 fiber measurements were used for the calculations. The evaluation of equations 4-1 - 4-3 made using these measurements give $\bar{l} = 146nm$ and $l = 186nm$. The calculated average thickness is 31.4 nm. However this value must be

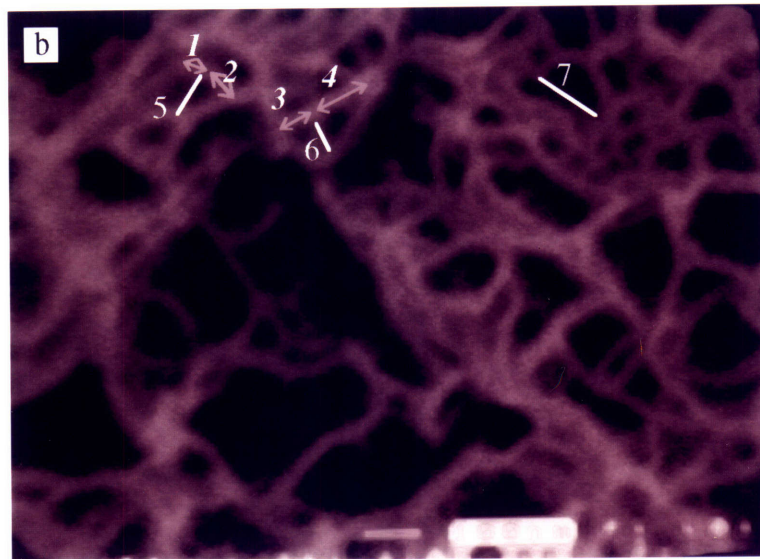
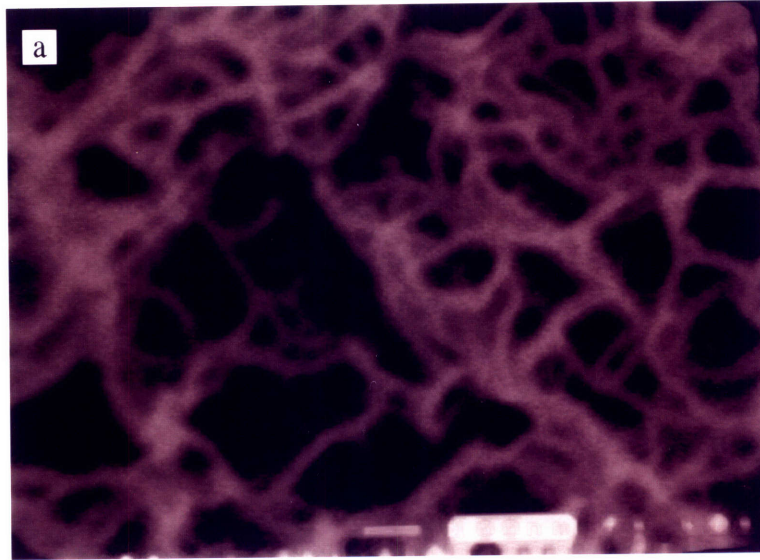


Figure 4.5. SEM's of EFK8 at 3.3 mg/ml and magnification of x100,000: a) original SEM and b) SEM with marked fibers.

corrected to account for the thickness of the gold-palladium coating. The coating has a thickness of 5 to 10 nm. This amount must be subtracted twice from the average thickness. This calculation gives a fiber thickness, t , that lies within the range of 11.4 to 21.4 nm. The values of t and l obtained, result in

$$\frac{t}{l} = 0.06 \text{ to } 0.12, \text{ and}$$

$$\frac{\rho^*}{\rho_s} = 0.01 \text{ to } 0.04.$$

The analysis for EFK at 10 mg/ml was done with the x100000 micrograph in Figure 4.3f.

It involved measurements from 58 fibers. The edge length measurements give $\bar{l} = 57\text{nm}$ and $l = 73\text{nm}$. The average fiber thickness was found to be 20.9 nm. The coating thickness for this sample is between 2 and 5 nm. The resulting corrected fiber thickness t ranges from 10.9 to 16.9 nm. These values give

$$\frac{t}{l} = 0.15 \text{ to } 0.23, \text{ and}$$

$$\frac{\rho^*}{\rho_s} = 0.07 \text{ to } 0.16.$$

The image analysis results for both specimens are summarized in Table 4.1.

Table 4.1. Image Analysis Results: EFK8

Concentration (mg/ml)	Thickness t (nm)	Length l (nm)	t/l	ρ^*/ρ_s
3.3	11.4 - 21.4	186	0.06 - 0.12	0.01 - 0.04
10	10.9 - 16.9	73	0.15 - 0.23	0.07 - 0.16

4.3.4 Discussion

The peptide materials studied exhibited a fibrous structure characteristic of cellular materials with no preferred alignment. This is reasonable given that the peptide molecules have estimated lengths of 3 to 6 nm. Since the injection device used to make the samples has characteristic length dimensions several orders of magnitude higher than these lengths, alignment was not expected.

The measurements made in the image analysis have several sources of error. It is important to bear in mind that the images obtained display the surface structure. The properties at the surface might differ from the bulk material properties. The surface of the material could experience deformations or mechanical insults that introduce artifices to its structure. For instance, anisotropy could be observed on the surface and not be present in the bulk material. For the samples studied, no significant anisotropy was noticed. However, the non-uniformities observed in EFK8 at 10 mg/ml could potentially be present only at the surface. The exact reason for the formation of these non-uniformities in the specimen is not known. It is possible that the tendency of the material to assemble is augmented at high concentrations. This might cause some extent of peptide self-assembly before exposure to the saline, leading to material aggregates. The variations and impurities on the peptide materials themselves will add to the error in the measurements. TEM is sometimes used for observation of cross-sections of specimens. This alternative might solve some of the obstacles mentioned and eliminate problems discussed earlier regarding the measurements of fiber dimensions. A better control of the coating thickness will also reduce the error in the measurements. This can be achieved by using an ion beam coater in place of a sputter coater.

The image analysis results show that a material's relative density is related to its concentration. The concentration gives the mass of peptide per volume of water in solution. Therefore, dividing it by the density of water should give a value comparable to the relative density. Solutions at concentrations of 3.3 and 10 mg/ml have 0.33 and 1% by mass of peptide, respectively. The relative density for the 0.33% solution from the image analysis is between 1 and 4%. For the 1% material the measured density lies between 7 to 16%. Both specimens have relative densities higher than their mass percentage. This could be due to the sources of error discussed in the analysis section. As explained earlier, the error in identifying junctions was expected to result in an overestimate of the densities. The discrepancy could also be the result of large amounts of water incorporated in the fibers. A large percentage of water in the fibers will cause the solid volume fraction to be much higher than the peptide mass percentage. The ratios of concentration and relative density should still be comparable. Since the fiber composition remains the same, the solid density is expected to remain constant. So the ratio of relative densities equals the ratio of matrix densities. This ratio, like the concentration ratio, depend only on the mass of peptide material per unit volume. The concentrations of 10 and 3.3 mg/ml EFK8 give a concentration ratio of 3.03. The relative densities of these materials, as presented in Table 4.1, have a ratio ranging from 1.70 to 14.40. So the concentration ratio lies within the range of relative density ratio. Median

range values of the relative densities give a ratio of 4.50. This density ratio of 4.50 and the concentration ratio of 3.03 are in considerable agreement.

4.4 References

1. Little, B., P. Wagner, R. Bay, R. Pope, R. Scheetz. "Biofilms: an ESEM evaluation of artifacts introduced during SEM preparation," *Journal of Industrial Microbiology*, Vol. 8, p. 213, 1991.
2. Verdon, S.L., E.L. Chaikof, J.E. Coleman, L. Hayes, R.J. Conolly. "Scanning electron microscopy analysis of polyethylene oxide hydrogels for blood contact," *Scanning Microscopy*, Vol. 2, 341-350, 1990.
3. Nation, J.L. "A new method using Hexamethyldisilazane for preparation of soft insect tissues for scanning electron microscopy," *Stain Technology*, Vol. 58, pp. 347-351, 1983.
4. Canby, C.A., U. Dogan, R.J. Tomanek. "Hexamethyldisilazane (HMDS) for mammalian tissue: An alternative method to critical point drying (CPD)," *Journal of Electron Microscopy Technique*, Vol. 2, p. 653, 1985.
5. Hayat, M.A. *Introduction to biological scanning electron microscopy*. Baltimore, Maryland: University Park Press, pp. 136-151, 1978.
6. Zhang, S., T.C. Holmes, C.M. DiPersio, R.O. Hynes, S. Xing, A. Rich. "Self-complementary oligopeptide matrices support mammalian cell attachment," *Biomaterials*, Vol. 16, pp. 1385-1393, 1995.
7. Gibson, L. J. and M. F. Ashby. *Cellular Solids*. New York: Pergamon Press, pp. 11-41, 1988.

Appendix 4.A

Preparation of Biological Sample for SEM Studies

PROTOCOL

Purpose:

Prepare a biological sample for SEM. This involves fixation, dehydration and drying of the sample.

Materials:

specimen, glutaraldehyde, plastic capsule with removable screen lids, ethanol, and Hexamethyldisilazane (HMDS), gold-palladium coating

Phosphate buffer saline (PBS) consisting of:

0.1M NaCl in de-ionized distilled water

0.5X10⁻³M of NaPO₄ buffer at pH 7

20 mg/L Congo Red dye

Equipment:

refrigerator at 4°C

Tousimis Atosamdri-814 CO₂ Critical-Point Drier

Edwards Evaporative Coater E306A

Procedure:

Stage 1: Fixation

1. Transfer the specimen to plastic capsule with screen on bottom submerged in PBS. Close the top of capsule with screen to allow fluid exchange while preventing loss of the specimen. The time required to do this should be kept to a minimum or if possible avoided at all to avoid air-drying and collapse of the specimen.

2. Transfer the capsule containing the specimen into solution of 2.5% of the fixative glutaraldehyde in PBS. The specimen must be completely immersed.

3. Place the capsule in fixative solution at 4°C for 2 hours.

4. Remove the capsule and immerse in PBS to wash out the fixative. Repeat the wash 2 times.

Stage 2: Dehydration

1. Prepare 50 ml solutions of 5%, 10%, 20%, 30%, 40%, 50%, 60%, 70%, 80%, 90% ethanol in PBS. Put 50 ml of 100% ethanol in another container.

2. Transfer capsule from PBS wash to the 5% ethanol solution. After 10 minutes transfer to next higher concentration, namely 10%. Keep repeating by transferring to next higher ethanol concentration after 10 minutes until the concentration of 100% ethanol is reached.

3. Leave capsule with specimen immersed in 100% ethanol until the final drying, presented in stage 3, is to be done.

Stage 3: Drying

Method 1: HMDS

1. Prepare a 50 ml solution of 50% ethanol in HMDS.

2. Transfer specimen capsule from 100% ethanol, as stated in step 3 of dehydration, to 50% ethanol in HMDS solution. Leave capsule immersed for ten minutes.

3. Remove capsule from ethanol-HMDS solution and immerse in 100% HMDS for ten minutes. Repeat 2 times to wash out all ethanol.

4. Remove sample from solution. Leave capsule exposed to air so the sample air-dries.

Method 2: CO₂ critical-point dry

1. Fill up drying chamber in the Autosamdri drier with 100% ethanol.

2. Move the specimen capsule from 100% ethanol, as stated in step 3 of dehydration, to the drying chamber, making sure it is completely immersed in ethanol.

3. Close drying chamber. Make sure the lid is tightly sealed

4. Open valve of CO₂ tank. Turn drying machine on and put on "Manual" operation by pressing the button labeled that way.

5. Press the "Cool" button. Cool light will go on. Wait 1 minute for chamber to cool.

6. Press the "Fill" button. Wait 1.5 minutes for the chamber to be filled with CO₂.

7. Press the "Purge" button. Wait 10 to 15 minutes for ethanol to be purged. The cool light will go off during purge. Purge is completed when the CO₂ comes out dry. This can be checked by holding paper against exhaust CO₂ and noticing whether the paper stays completely dry.

6. Release the "Purge" button and press "Heat." Wait several minutes until the CO₂ critical point is reached. The heat indicator light will go off when this happens.

7. Wait 5 to 10 minutes after heat indicator light goes off. Then release the "Heat" button.

8. Press the "Bleed" button and close valve of the CO₂ tank. Submerge exhaust tubing in beaker full of water so CO₂ bubbles can be observed. Adjust the bleed knob so that the bubbles come out at a rate that allows them to be counted. This process should be held as the pressure goes from 8000 kPa to 0 kPa. It takes approximately 20 minutes. The slow decompression avoids the damage the specimen could experience under sudden decompression (1).

9. Transfer the dried specimen to a desiccator where it should be stored until it is coated and studied with the SEM.

Stage 4: Coating

1. Place specimens on the coating machine mounting stage and place over samples.

2. Turn on coater and penning gauge. Wait for appropriate vacuum. Add liquid N₂ to cold trap.

3. Start specimen motor and set rotation rate. Reset power control. Position shutter between source and sample.

4. Slowly turn up power control to the melting temperature of the coating metal. When metal has melted, move shutter aside and slowly increase current to evaporation heat. At this point the sample will be coated.

5. When coating is complete, move shutter between source and sample. Turn power control to zero.

6. When filament has cooled to a temperature below the evaporation temperature, turn rotation motor off. Wait a few minutes for filament to cool.

7. Turn valve control lever to backing position. Remove cover and samples.

8. Transfer the dried specimen to a desiccator where it should be stored until it is studied with the SEM.

References

1. Hayat, M. A. Introduction to biological scanning electron microscopy. Baltimore, Maryland: University Park Press, pp. 136-151, 1978.

Appendix 4.B

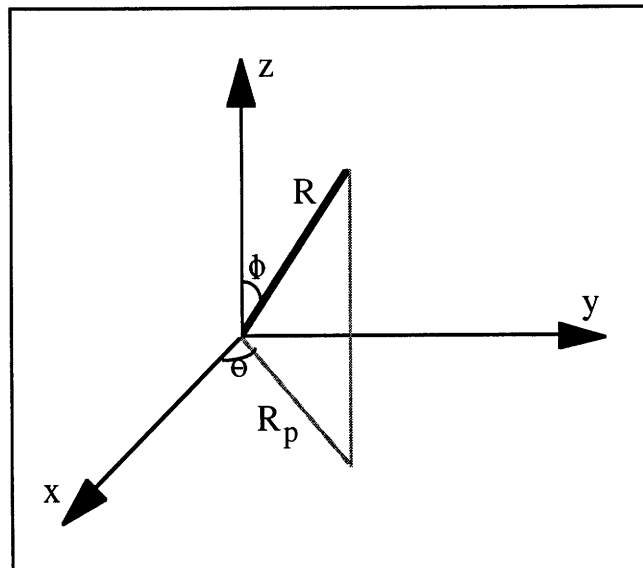
Calculation of Correction Factor for Mean Fiber Length Measurement

DERIVATION

To determine the correction fiber of fiber mean length, it is assumed that the fibers are randomly oriented in space. The fibers are assumed to have a length R . Its projected length on a plane, R_p , is given by

$$R_p = R \sin(\phi) \quad (\text{B-1})$$

where ϕ is the angle between R and the Cartesian axis perpendicular to the plane of projection. This is illustrated below.



The measurement of the fiber projections will result in average projected length, \bar{l} , different from the average of actual fiber lengths. The ratio \bar{l} to the actual length average, l , is given by

$$\frac{\bar{l}}{l} = \frac{2 \int_{-\frac{\pi}{2}}^{\frac{\pi}{2}} \int_0^{\pi} \int_0^R r^2 \sin^2(\phi) dr d\theta d\phi}{2 \int_{-\frac{\pi}{2}}^{\frac{\pi}{2}} \int_0^{\pi} \int_0^R r^2 \sin(\phi) dr d\theta d\phi} . \quad (\text{B-1})$$

This expression simplifies to

$$l = \frac{4}{\pi} \bar{l} . \quad (\text{B-2})$$

Therefore, a correction factor of $4/\pi$ is required for the mean length calculation from the mean projected length.

Chapter 5

Mechanical Properties

5.1 Introduction

The successful use of biomaterials in medical science requires a detailed knowledge of their physico-mechanical properties. The mechanical properties greatly influence the materials' functionality and performance. Therefore, these properties must be quantified to determine the viability of the materials for specific applications. The relevant mechanical parameters can be determined by conducting a series of mechanical tests on the materials. One such test is the tensile test. This test is commonly performed to evaluate important properties such as the Young's modulus and the fracture strength.

This chapter discusses the tensile testing of the ionic self-complementary oligopeptide biomaterial EFK8. It begins with background information on the mechanical testing of biological tissues and biomaterials. This information is followed by a description of the apparatus used for the fabrication and mechanical testing of oligopeptide materials. A modeling of the diffusion-controlled assembly process during specimen fabrication is presented. Finally, the chapter includes the results for the tensile tests of EFK8 at various concentrations.

5.2 Background

Biomaterials used in medical science must possess a variety of physical, mechanical, and chemical properties to meet the functional requirements of different applications. In many medical techniques, one of the main purposes of biomaterials is to provide mechanical and structural support for cells and tissues. As a result, a quantified mechanical characterization of the biomaterials and the tissues involved is essential prior to clinical usage. The mechanical properties relevant to use in medical science can be obtained from a variety of tests. Two useful and common tests are the tensile test and the fatigue test. Tensile tests and quasi-static tests are used to obtain the stress-strain behavior of the material. The resulting data can be used to determine parameters relevant to the mechanical compatibility and stability of the material (1, 2). These parameters include properties such

as the tensile modulus and fracture strength. Fatigue tests are used to evaluate endurance related properties such as fatigue strength. They also give an indication of the mechanical properties under dynamic loading conditions (1). Other tests are used to characterize the time dependent material behavior of viscoelastic materials. Among these are tests to determine the stress-relaxation, creep, and response to vibratory loads, which give additional information consequential to the medical use of biomaterials in medicine (1, 2, 3).

The mechanical testing of biomaterials and biological tissues presents needs that cannot be addressed by standard testing equipment. Additional testing requirements necessitate the modification of existing machines as well as the development of new specialized experimental devices. One challenge that arises when testing some biomaterials is the need to use small-scale specimens. Biomaterials are often available only as small samples during the development stage. The use of large specimens can sometimes make specimen fabrication difficult or costly. As a result, many of the systems developed for biomaterials' testing are small-scale testing devices (1, 2, 3). An example of such systems is the small scale tensile creep testing machine developed by Ker (2). It uses a length transducer to measure the extension of loaded polymer samples as a function of time. Another small-scale system uses a stepper motor and ball screw to apply strains and a load cell to measure resulting forces (3). This system was designed for compression tests and creep tests. Other equipment incorporates the capacity to apply dynamic loads. An example of these machines is the miniature servo-hydraulic testing machine developed by Hayashi (1). It uses a vidicon displacement analyzer and a load cell to monitor the respective strain deformations and forces on a specimen. Materials tested with the device include human abdominal aorta, canine femoral vein and various elastomers (1). Additional testing challenges result when materials need to be tested while immersed in an aqueous medium. This might be required to prevent collapse of hydrated materials or to simulate *in vivo* conditions. The machine built by Ker allows the containment of test specimens in a fluidic bath during testing (2).

The mechanical testing of ionic self-complementary oligopeptide biomaterials presented various requirements that could not be met by standard testing machines. The use of small specimens was preferred over large specimens. It simplifies the specimen fabrication process and diminishes the problems of availability of large amounts of the material. Furthermore, the hydrated nature of the materials imposed the necessity to have the specimen continuously submerged in an aqueous medium. Transferring a fabricated sample to the testing machine and grasping its ends for stretching without material failure or collapse would provide additional difficulties. A small scale mechanical testing system was

developed and constructed for the mechanical testing of this class of biomaterials (4). The system can be used for the fabrication of tensile test specimen in an aqueous medium. It allows the conduction of uniaxial tensile testing in that medium without requiring movement of the specimen. A detailed description of the apparatus and its specifications are included in the text documenting the system's development and use (4). A summary of the most important features is presented in the next section.

5.3 Mechanical Testing Device

5.3.1 System Description

A schematic and a picture of the system developed for specimen fabrication and tensile testing are included in Figure 5.1 and Figure 5.2, respectively. The peptide biomaterial is fabricated by injection of peptide solution into a tank filled with saline solution. The tank consists of a clear polystyrene cuvette. The composition of the 0.1 M saline solution, PBS, is specified in Appendix 4.A. The peptide is injected into the saline via a stainless steel needle tip using a syringe pump. This needle is mounted on a translating plate connected to a motorized micrometer table. The translating plate is retracted as the peptide is injected so there is no motion of the peptide with respect to the saline. Adjustments of the injection flowrate and retracting needle speed allow the regulation of the cross-sectional area of the of cylindrical peptide specimen.

The specimen fabricated for tensile tests is dog bone shaped. The neck, or middle part of the bone, is a section of reduced cross-sectional area that is monitored to measure the stress corresponding to a given strain. To fabricate the specimen, peptide solution is injected against a receptacle in the bottom of the tank or cuvette. The partial hydrophobicity of the peptides result in adhesion of the peptide material to the plastic bottom of the cuvette and the edges of the receptacle. This hydrophobic adhesion provides the bottom grip or anchor for the stretching of the specimen during tensile testing. A plastic or a stainless steel mesh can be used as receptacles. As the peptide is injected the needle is retracted, resulting in a cylindrical peptide matrix. To make the neck, the speed of the motor moving the retracting micrometer table is increased while the injection flowrate is kept constant. The speed increase results in a decrease of cross-sectional area which leads to the formation of the specimen neck. Once the neck is formed, the motor speed is decreased to its original value. This will result in an upper part of cross-section similar to the bottom part of the specimen. Once the specimen is complete, the pump and the retracting motor are turned off. The matrix assembly in the needle tip results in adhesion of the material to the tip. This adhesion provides the upper

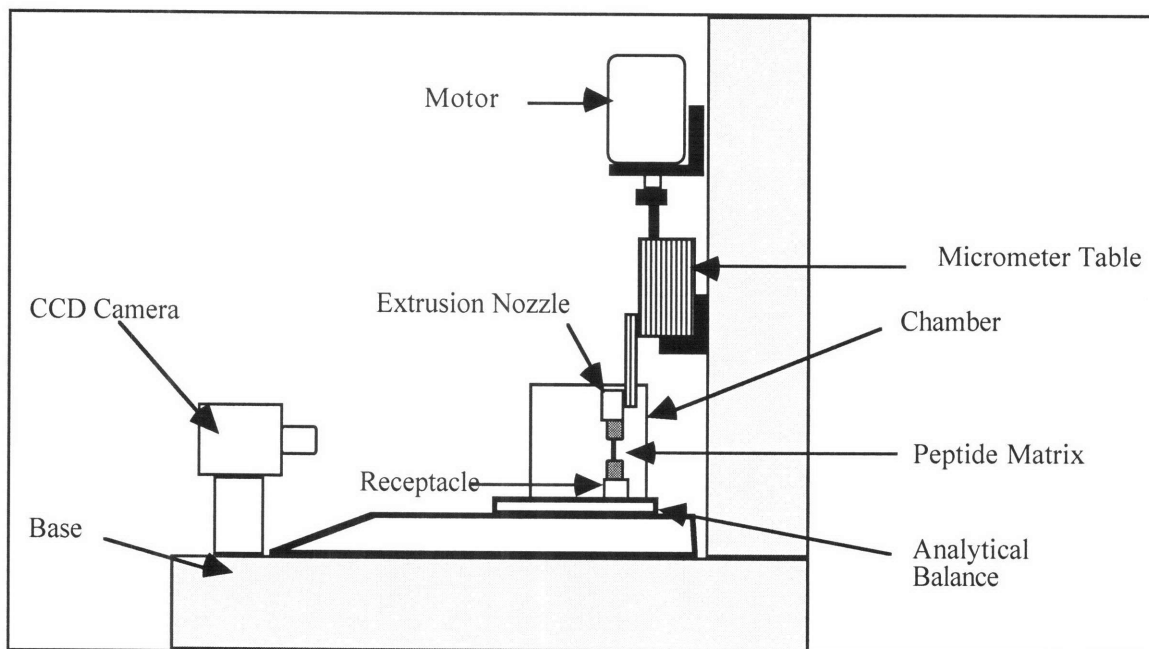


Figure 5.1. Schematic of tensile testing system

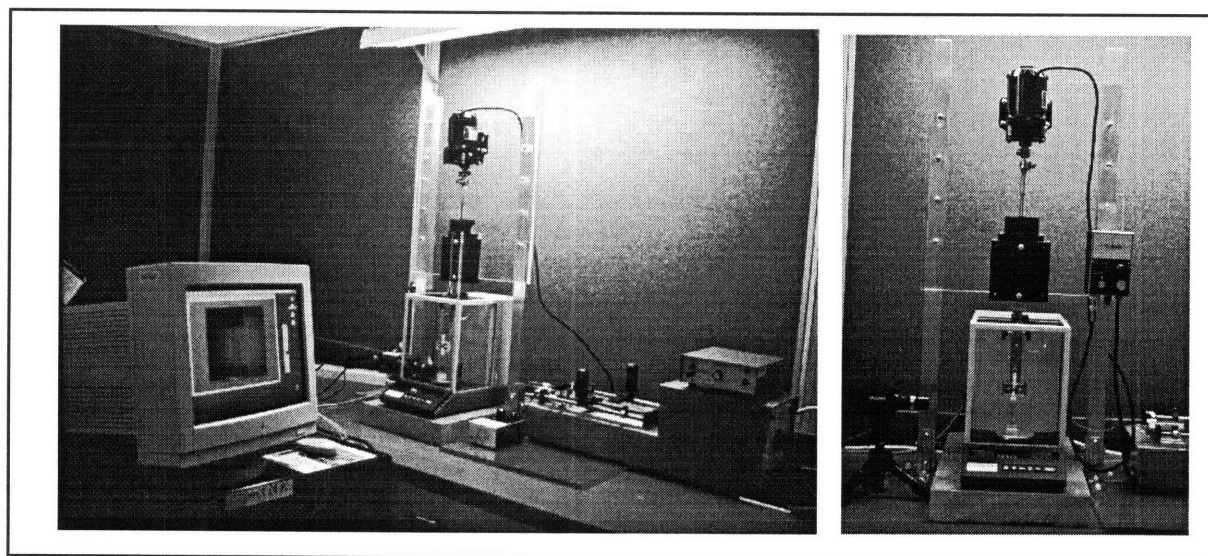


Figure 5.2. Pictures of tensile testing system

grip for the tensile test. A picture of a dog bone shaped specimen is included in Figure 5.3.

The tensile test is conducted by subjecting the specimen to incremental strains. The strains are applied by moving the retracting needle upwards. The motor that moves the retracting needle is turned on for a short time interval, causing the needle to retract by approximately 0.013 mm. Since the specimen is "anchored" at both ends by adhesion to the needle and receptacle it elongates or stretches. The steady state force resulting from the fixed displacement is registered by the balance on which the saline tank lies. The strains are monitored by capturing digital pictures of the neck of the specimen with a CCD camera interfaced to a computer. This process of applying strains and recording resulting forces and specimen images is repeated until the specimen fails. The strains are measured from the images captured. By tracking "particles," or specks, in the textured surface of the material, the amount of stretching can be determined. The resulting data are used to generate stress-strain curves.

5.3.2 Specifications

The apparatus specifications are presented in detail in the documentation of its development and design (4). The digital images of the specimen were obtained using a Pulnix TM-97000 CCD interfaced to a Macintosh 8500. The process parameters involved in the fabrication of the specimen are the injection flowrate, Q , and the retracting needle speed, V . The values used were $0.097 \text{ mm}^3/\text{sec}$ for flowrate and $65 \text{ }\mu\text{m}/\text{sec}$ for speed. The resulting specimen had bottom and top anchors of 2 mm in length and 1.6 mm in diameter. The specimen neck had an approximate length and diameter of 8 mm and 1.38 mm, respectively. The images used to measure lengths and displacements can resolve $7.3 \text{ }\mu\text{m}$. For the given neck diameter, the cross sectional area is $1.54\text{E-}6 \text{ m}^2$. The length resolution of $7.3 \text{ }\mu\text{m}$ results in an area measurement uncertainty of 1%. The length monitored for strain measurements is approximately 0.8 mm. The uncertainty introduced in strain measurements is $9\text{E-}3$, or .9%, elongation. As a result, strains in the order of 1% have a significant uncertainty of 90% of its value. The uncertainty decreases for larger strains. A strain of 10% will have an uncertainty of 9% of the measured quantity. The balance used to measure resulting forces on the specimen has a resolution of 0.1 mg. This resolution correspond to a force of $9.8\text{E-}7 \text{ N}$. The forces measured in the experiments ranged mostly from $9.8\text{E-}6$ to $2\text{E-}4 \text{ N}$. This range corresponds to stresses from 6 to 127 Pa. The uncertainties in these stress measurements go from 1 to 10%, with higher uncertainties resulting from smaller stresses. The error in stress and strain measurement

propagates in the calculation of Young's modulus. The magnitude of the resulting error depends on the stresses and strains involved in the calculation. It is dominated by the resolution error in strain. Therefore, it will be larger for smaller strains. Since the stiffer materials results in smaller strains for a given stress, they will exhibit the larger error. The propagated uncertainty in Young's modulus is approximately 30%, or about 4 kPa for the stiffer materials tested.

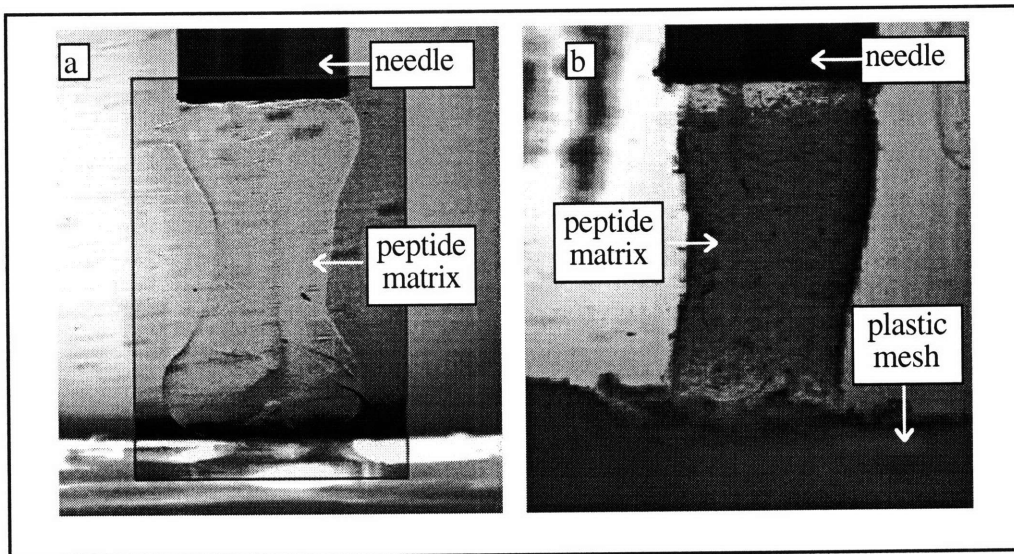


Figure 5.3. Picture of tensile test specimens: a) specimen after fabrication (shaded box shows enhanced contrast to allow observation of colorless specimen), b) specimen anchored to plastic mesh (Congo red stain allow observation of particles on the specimen)

5.4 Diffusion-Controlled Assembly Model

5.4.1 Peptide Fabrication Process

The peptide matrix is fabricated by injecting peptide solution into a monovalent salt solution, PBS. The injected peptide is in a liquid form. As the salt from the injection medium diffuses into the peptide solution, the peptide self-assembles and solidifies. While the peptide solution is injected into the saline, the needle is moved in a direction opposing the peptide velocity. The speed of the needle is equal to the peptide's injection speed. As a result, there is no motion of the peptide solution with respect to the saline. This process

is illustrated in Figure 5.4. A diffusion model of the self-assembly process is presented in the following section.

5.4.2 Diffusion Model

The mass transfer of salt taking place during the fabrication of the peptide is modeled as steady state diffusion in a two-region concentric cylinder. The two regions are the peptide cylinder and the saline annulus surrounding the peptide. The saline has an initial salt concentration of 0.1M, while the peptide starts with a salt concentration of zero. The salt from the saline diffuses into the peptide solution during specimen fabrication leading to macroscopic self-assembly. Two different diffusion models are presented. The first one consists of modeling the peptide region as the Graetz problem. In this model, it is assumed that the salt concentration at the interface of the two regions remains equal to the initial saline concentration. Since mass transfer in the saline region is neglected, only the peptide region is considered in the analysis. Also, the velocity of the needle is neglected. Thus the model represents injection of the peptide into stationary saline. In the second model, the mass transfer in both regions is taken into account. The two-region diffusion model represents a process closer to the real peptide fabrication. It incorporates the velocity of the needle as well as the diffusion in the saline. The two models are presented in the next sections.

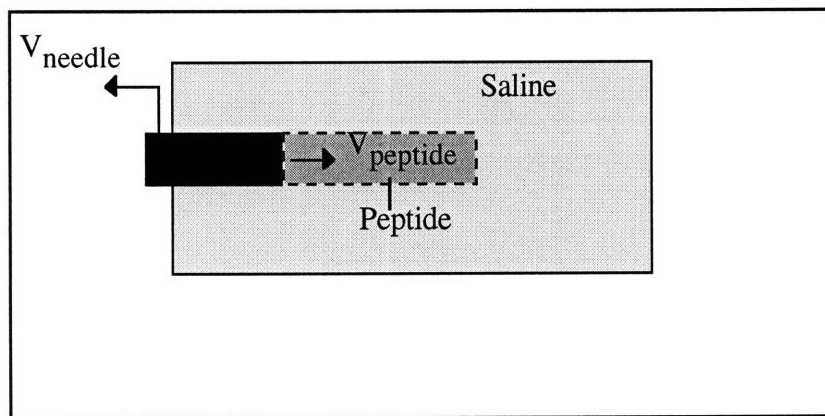


Figure 5.4. Fabrication of Oligopeptide

5.4.2A Model 1: The Graetz Problem

The first model represents steady state mass transfer in laminar flow through a tube that consists of the peptide cylinder. It is assumed that the flow is fully developed and axial

diffusion is neglected. The inlet salt concentration is ρ_i . The concentration at the tube wall is equal to the saline concentration ρ_w . A schematic of the problem modeled is presented in Figure 5.5. The governing equation for this diffusion problem is given by conservation of species. The conservation of salt species, or species A, is given by

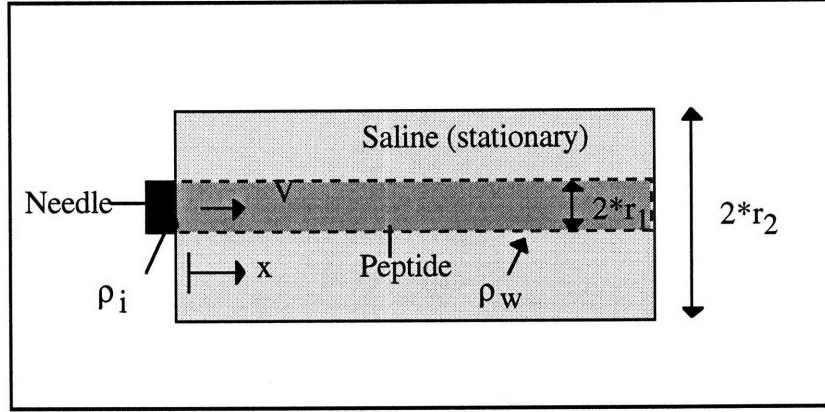


Figure 5.5. Peptide Fabrication Diffusion Model : Graetz Problem

$$V \frac{\partial \rho_A}{\partial x} = D \left(\frac{\partial^2 \rho_A}{\partial r^2} + \frac{1}{r} \frac{\partial \rho_A}{\partial r} \right) \quad (1)$$

where V is the peptide speed relative to the needle, ρ_A is the concentration of species A, x is the axial coordinate, D is the diffusion constant of species A in the peptide solution, and r is the radial coordinate.

The boundary conditions for this problem are given by

$$\rho_A \Big|_{r=r_1} = \rho_w \quad (2)$$

$$\rho_A \Big|_{x=0} = \rho_i \quad (3)$$

Equations 1-3 can be solved by separation of variables. First equations 1-3 are rewritten in terms of the dimensionless variable Θ , which is defined as follows

$$\Theta = \left(\frac{\rho_w - \rho_A}{\rho_w - \rho_i} \right) \quad (4)$$

So equations 1-3 become

$$V \frac{\partial \Theta}{\partial x} = D \left(\frac{\partial^2 \Theta}{\partial r^2} + \frac{1}{r} \frac{\partial \Theta}{\partial r} \right) \quad (5)$$

$$\Theta|_{r=r_1} = 0 \quad (6)$$

$$\Theta|_{x=0} = 1 \quad (7)$$

The solution to equations 5-7 is given by

$$\Theta = \sum_{j=1}^{\infty} \frac{2 J_0(b_j r)}{b_j r_1 J_1(b_j r_1)} \exp\left(\frac{-D b_j^2 x}{V}\right) \quad (8)$$

Rewriting equation 8 in terms of the variables in equations 1-3 gives

$$\rho_A = \rho_w + (\rho_i - \rho_w) \left(\sum_{j=1}^{\infty} \frac{2 J_0(b_j r)}{b_j r_1 J_1(b_j r_1)} \exp\left(\frac{-D b_j^2 x}{V}\right) \right) \quad (9)$$

where J_0 and J_1 are Bessel functions of the first kind of degree 0 and 1, respectively. The eigenvalues b_j are given by

$$J_0(b_j r_1) = 0 \quad (10)$$

The numerical values of the parameters for the peptide fabrication in equations 8-10 are $V=6.5E-5$ m/s, $r_1=.69E-3$ m, and $D=1.62E-9$ m²/s. The value of D is an approximation for peptide solutions at very low concentrations. It corresponds to the diffusion of salt in water. The salt concentration at the wall is assumed to be equal to the initial saline concentration. A plot of the centerline concentration of the peptide at the end of fabrication is included in Figure 5.6. The plotted curve correspond to truncation of the series solution to the first 20 terms.

5.4.2B Model 2: Two-Region Diffusion

The second model developed represents diffusion mass transfer in a two-region concentric cylinder. In this model both the peptide and the saline move with respect to the needle. Their respective speeds are V_1 and V_2 . Since this model incorporates the mass transfer in the saline, the concentration at the peptide-saline interface is not constant. The governing equations result from applying conservation of species in the form presented in equation 1 to each of the two regions. They are given by

$$V_j \frac{\partial \rho_j}{\partial x} = D_j \left(\frac{\partial^2 \rho_j}{\partial r^2} + \frac{1}{r} \frac{\partial \rho_j}{\partial r} \right) \quad j=1,2 \quad (11)$$

In equation 11, ρ still refers to the concentration of species A. The subscript A has been dropped for simplicity in notation. The new subscript j indicates the region. The notation used consists of j equal to 1 for the peptide cylinder and 2 for the saline annulus. Thus the

peptide and the saline have corresponding velocities V_1 and V_2 and corresponding diffusion constants D_1 and D_2 . As in the previous section, equation 11 can be re-written using the dimensionless quantity Θ as defined in equation 4. That gives the governing equations

$$V_j \frac{\partial \Theta_j}{\partial x} = D_j \left(\frac{\partial^2 \Theta_j}{\partial r^2} + \frac{1}{r} \frac{\partial \Theta_j}{\partial r} \right) \quad j=1,2$$

$$\Theta = \begin{cases} \Theta_1 & 0 \leq r \leq r_1 \\ \Theta_2 & r_1 \leq r \leq r_2 \end{cases} \quad (12)$$

where r_1 is the peptide matrix radius and r_2 is the saline tank radius. The first boundary condition is given at the entrance, where x equals 0. At this location the concentration equals ρ_i for the peptide, or region 1, and ρ_w for the saline, or region 2. This boundary condition is expressed by

$$\Theta|_{x=0} = \begin{cases} 1 & 0 \leq r \leq r_1 \\ 0 & r_1 \leq r \leq r_2 \end{cases} \quad (13)$$

The second boundary condition consists of fixed salt concentration at the outer radius of the saline, r_2 , which is at a radial distance of infinity. This boundary condition is modeled by letting the concentration at r_2 equal to ρ_w and letting r_2 be much greater than r_1 . This boundary condition is given by

$$\Theta|_{r=r_2} = 0 \quad (14)$$

Two more boundary conditions arise from continuity of concentration and concentration flux at the interface of the two regions. These constraints are given by

$$\Theta_1|_{r=r_1} = \Theta_2|_{r=r_1} \quad (15)$$

$$D_1 \frac{\partial \Theta_1}{\partial r} \Big|_{r=r_1} = D_2 \frac{\partial \Theta_2}{\partial r} \Big|_{r=r_1} \quad (16)$$

The set of governing equations, labeled as equation 12, can be solved by separation of variables. The solutions have the form

$$\Theta_1 = \sum_{n=1}^{\infty} A_n J_0(b_{1n}r) \exp\left(\frac{-D_1 b_{1n}^2 x}{V_1}\right) \quad (17)$$

$$\Theta_2 = \sum_{n=1}^{\infty} A_n B_n (J_0(b_{2n}r) + C_n Y_0(b_{2n}r)) \exp\left(\frac{-D_2 b_{2n}^2 x}{V_2}\right) \quad (18)$$

where J_o and Y_o are the Bessel functions of degree zero of the first and the second type, respectively. An additional condition results from the fact that the x behavior at the interface should be the same on either region. This condition gives

$$\frac{D_1 b_{1n}^2}{V_1} = \frac{D_2 b_{2n}^2}{V_2} \quad (19)$$

Applying conditions 14-16 and 19 to equations 17-18 give the values for B_n , C_n , b_{1n} , and b_{2n} . Then A_n is obtained by applying the condition given in equation 13 to the solutions given in equations 17-18. The expression for A_n is given by

$$A_n = \frac{V_1 \int_0^{r_1} \Theta_1|_{x=0} r J_o(b_{1n} r) dr + V_2 \int_{r_1}^{r_2} \Theta_2|_{x=0} r B_n (J_o(b_{2n} r) + C_n Y_o(b_{2n} r)) dr}{V_1 \int_0^{r_1} r J_o^2(b_{1n} r) dr + V_2 \int_{r_1}^{r_2} r B_n^2 (J_o(b_{2n} r) + C_n Y_o(b_{2n} r))^2 dr} \quad (20)$$

For the peptide specimen fabrication process V_1 and V_2 equal V . Similarly, D_1 and D_2 equal D . That gives

$$b_{1n} = b_{2n} = b_n \quad (21)$$

$$B_n = 1 \quad (22)$$

$$C_n = 0. \quad (23)$$

The eigenvalues b_n are given by

$$J_o(b_n r_2) = 0. \quad (24)$$

The expression for the coefficients A_n in equation 20 simplifies to

$$A_n = \frac{2J_1(b_n r)}{r_1 b_n (J_o^2(b_n r_1) + J_1^2(b_n r_1))} \quad (25)$$

Therefore, the solution to the diffusion model is given by

$$\Theta = \sum_{n=1}^{\infty} A_n J_o(b_n r) \exp\left(\frac{-D b_n^2 x}{V}\right) \quad (26)$$

where b_n and A_n are as indicated in equations 24 and 25, respectively.

The results from the two diffusion models are depicted in Figure 5.6. As in the Graetz model, the numerical values of the parameters for the peptide fabrication in equations 24-26 are $V=6.5E-5$ m/s, $r_1=.69E-3$ m, and $D=1.62E-9$ m²/s. Also, the inlet salt concentration in the peptide solution, ρ_i , is zero. The value of r_2 is set equal to 3 times the value of r_1 . This figure presents a plot of the concentration ratio ρ_A/ρ_w at the centerline for the given parameter values. The solution for both models was truncated to include only the first twenty terms of the infinite series.

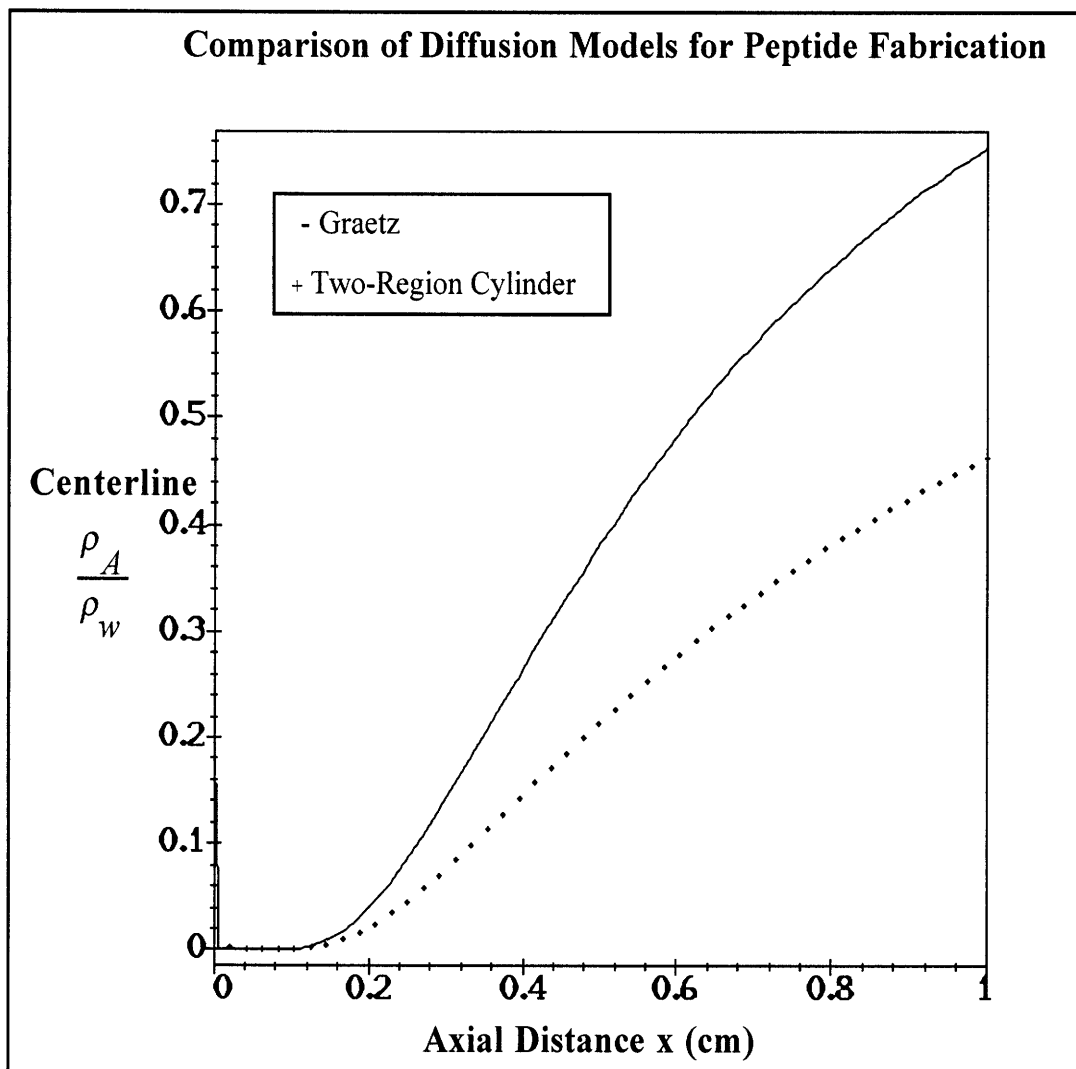


Figure 5.6: Diffusion Model Comparison

The plot in Figure 5.6 shows that both models predict a salt concentration increase with axial distance in the peptide region. The concentration starts at zero at the entrance and gradually increases to approach the saline concentration ρ_w . This increase is faster for the Graetz model because it neglects the mass transfer in the saline and sets the concentration at r_1 equal to ρ_w .

As mentioned before, the boundary condition at a radial distance of infinity in the two-region model was imposed by using an arbitrary outer radius r_2 . The outer radius can be given a large value to approximate the desired boundary condition. The results for this model with three different values of r_2 are shown in Figure 5.7. The depicted values of r_2 are $3r_1$, $10r_1$, and $20r_1$. The curves represent truncation of the series solution to 20 terms.

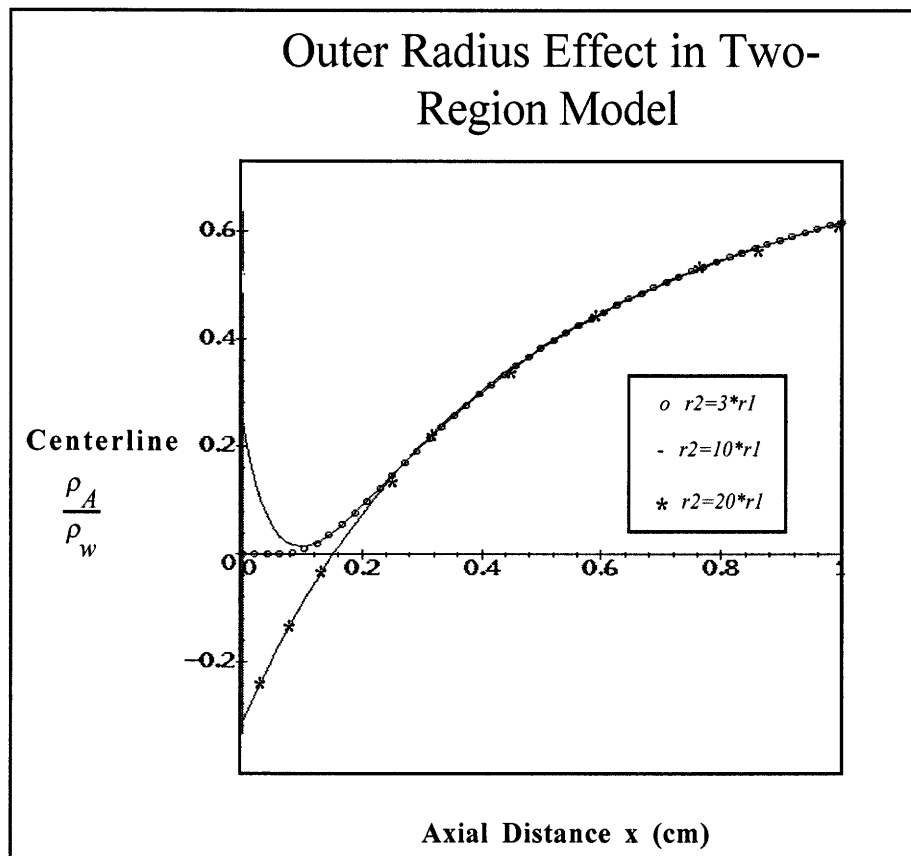


Figure 5.7. Effect of Outer Radius in Model Prediction

Figure 5.7 illustrates the similarity between the three different the curves corresponding to the different values of r_2 . The curve for an outer radius of $3r_1$ shows the desired behavior,

namely salt concentration of zero at the entry region and increase towards a concentration of ρ_w . The other two values of r_2 do not show the correct behavior at the entrance. However, the two curves do match the behavior predicted by $r_2 = 3r_1$ for larger values of the axial distance x . Thus the truncated series solution deviates from the desired behavior for very large values of r_2 . They approach the desired solution as x increases but show large error near the entrance. This error increases with increase in outer radius r_2 . The source of this error is the truncation used in the series solution. As seen in equation 24, the eigenvalues in the solution are obtained by dividing the roots of the Bessel equation of zero degree by r_2 . Thus, the increase in r_2 makes higher valued roots significant for low axial distances. However, Figure 5.7 shows that a value of $3r_1$ gives the desired approximate solution.

The curve shown in Figure 5.7 indicates the salt concentration in the centerline of the peptide specimen as a function of axial distance. The curve shows that the centerline concentration goes from 0 to 60% of the saline concentration as the distance from the needle increases from 0 to 1 cm. Since assembly of EFK8 occurs at concentration above approximately 20% of the saline concentration, most of the specimen is expected to assemble or solidify during the fabrication process. As a result, a solid and stable specimen of uniform cross section is easily obtainable for the given process parameters. However, since the resulting matrix will retard diffusion, more time exposure to the saline is allowed for complete assembly. Furthermore, salt must diffuse into the needle to induce assembly and peptide adhesion to the needle tip. Also, since the specimen is transparent, staining of the matrix is necessary for particle tracking during strain measurements. The staining becomes observable after over 30 minutes. More time is required for a sufficiently dark staining by the Congo red. For these reasons, a period of one and a half hours is allowed between specimen fabrication and tensile testing.

5.5 Tensile Test Results

Tensile tests were performed on EFK8 specimens at concentrations of 2.7, 3.3, 5.4, and 10 mg/ml. The stress-strain curves for these tests are included in figures 5.8 - 5.12. The first figure, Figures 5.8, illustrates the method used to calculate the strains for these curves. In this figure, four curves are shown. The curves labeled Strain 1, Strain 2, and Strain 3, correspond to strain measurements done at three different locations within the tensile specimen. The fourth curve, labeled Average Strain, depicts the stress-strain behavior that resulted from averaging the three strain calculations. This averaging of three strain measurements was used to eliminate some of the noise due to experimental error. This noise is clearly observed in the top three curves for EFK8 at 3.3 mg/ml in Figure

5.10. These three curves are based on a single strain measurements and do not include averaging. Due to the error involved in the measurements, the curves show substantial jumps in stress without change in strain and viceversa. These three curves also involved a lower resolution in strain measurements. The lower curve in Figure 5.10 and the curves in Figures 5.9 - 5.11 represent the average of three strain measurements and involve the resolutions indicated in the specifications section. The curve resulting from the averaging of strains in Figure 5.8 is included with the other 2.7 mg/ml data in Figure 5.9.

The three curves in Figure 5.9 suggest that the stress-strain behavior of the peptide material at 2.7 mg/ml is linear. The material exhibits linear stress-strain behavior all the way to fracture. Therefore, it behaves as a brittle material that fractures without noticeable plastic deformation. The Young's modulus was obtained from the slope of the least squares linear regression for stress versus strain. The three curves give Young's moduli values of 1.52, 1.61, and 1.63 kPa. Two of the three curves include data all the way to fracture. In both cases, fracture occurred in the middle region of the specimen. These two curves give fracture strengths of 44 and 57 Pa. The corresponding elongations at fracture are 3 and 3.4%. A substantial variation is expected in the fracture strength and strain to fracture obtained from the experiments. Since the data are obtained at incremental elongations rather than in a continuous fashion, the strength and fracture strain are approximated by the values for the last increment before fracture. The fracture will occur in the transition during the subsequent increment. Thus, the exact fracture point on the curve will not be acquired.

Figure 5.10 illustrates the stress-strain curves for peptide concentration of 3.3 mg/ml. As mentioned earlier, these curves showed substantial scatter. This scatter makes it hard to establish the linearity of the stress-strain behavior. However, the lowest curve, which involves higher resolution and strain averaging, indicates linear behavior. For purposes of comparison, the values of Young's moduli were calculated from the slope of a least squares linear regression, as was done for all other concentrations. The resulting Young's moduli are 2.67, 2.68, 2.94, and 3.32 kPa. The fracture strengths are approximately 119, 157, 211, and 218 Pa. The strains to fracture measured are 4.4, 4.8, 6.5, and 7.8 %. The specimens with moduli of 119 and 218 fractured in the narrow section. The other two fractured near the needle tip. Figure 5.11 includes the results for a concentration of 5.4 mg/ml. The calculated moduli are 5.0, 6.53, and 7.2 kPa. Only one experiment went all the way to fracture, resulting in fracture strength and elongation of 123 Pa and 1.7%, respectively. This stress- strain curve also exhibits linear behavior.

The highest concentration of EFK8 tested was 10 mg/ml. The results for tests at this concentration are illustrated in Figure 5.11. At this concentration, the material is

significantly stiffer than at the lower concentrations. The curves show significant jumps and erratic decreases in elongations for increases in stresses. Consequently, linearity is hard to establish. These jumps suggests the need of better resolution for the stiffer material. The range of strains over which data were acquired is much smaller for this concentration. The elongations at fracture are of 1.1 and 1.3%. These two specimens fractured in close to the bottom anchor. The elongation values are close to the strain measurement resolution. Therefore, uncertainty in measurements results in a large propagation of error. The Young's moduli for the material, as given by slope of the least squares linear fits, are 14 and 15.4 kPa. The peptide material exhibited fracture strengths of 162 and 231 Pa. Extensive data and improved resolution will be required to establish with certainty the linear stress-strain behavior. However, the present results suggest that the material is elastic-brittle.

The results from the mentioned experiments are summarized in Table 5.1. This table presents the elastic modulus, fracture strength, and strain to fracture at the four concentrations tested. The results are presented as a range and as an average. The number of data points used, n, is included in parenthesis.

Table 5.1. Tensile Tests Data for EFK8

Concentration (mg/ml)	Modulus (kPa)		Strength (Pa)		Elongation (%)	
	Range	Average	Range	Average	Range	Average
2.7	1.52 - 1.63	1.59 (n=3)	44 - 57	50.5 (n=2)	3.0 - 3.6	3.3 (n=2)
3.3	2.67 - 3.32	2.90 (n=4)	119 - 218	176.3 (n=4)	4.4 - 7.8	5.9 (n=4)
5.4	5.0 - 7.3	6.23 (n=3)	123	123 (n=1)	1.7	1.7 (n=1)
10	14.0 - 15.4	14.7 (n=2)	162 - 231	196.5 (n=2)	1.1 - 1.3	1.2 (n=2)

These data show trends in the dependence of tensile properties on concentration. The Young's modulus increases with increase in concentration. The fracture strength also exhibits the tendency to increase with concentration. The elongation, however tends to decrease with material concentration. A detailed analysis of the effect of concentration on the tensile properties, based on cellular solid theory, is presented in Chapter 6.

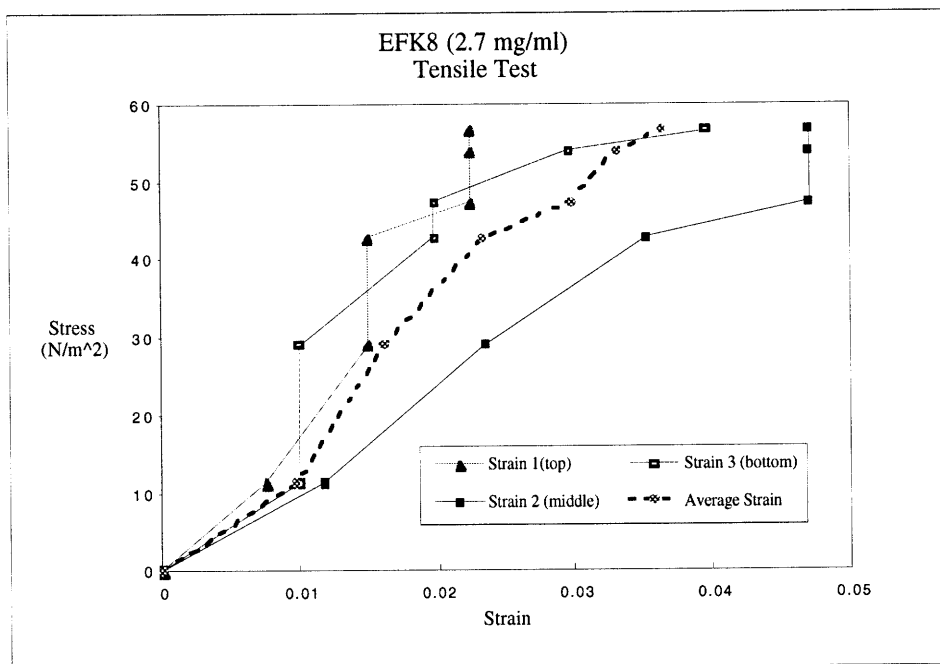


Figure 5.8. Averaging strain technique for stress-strain curves. Tensile test of EFK8 at 2.7 mg/ml.

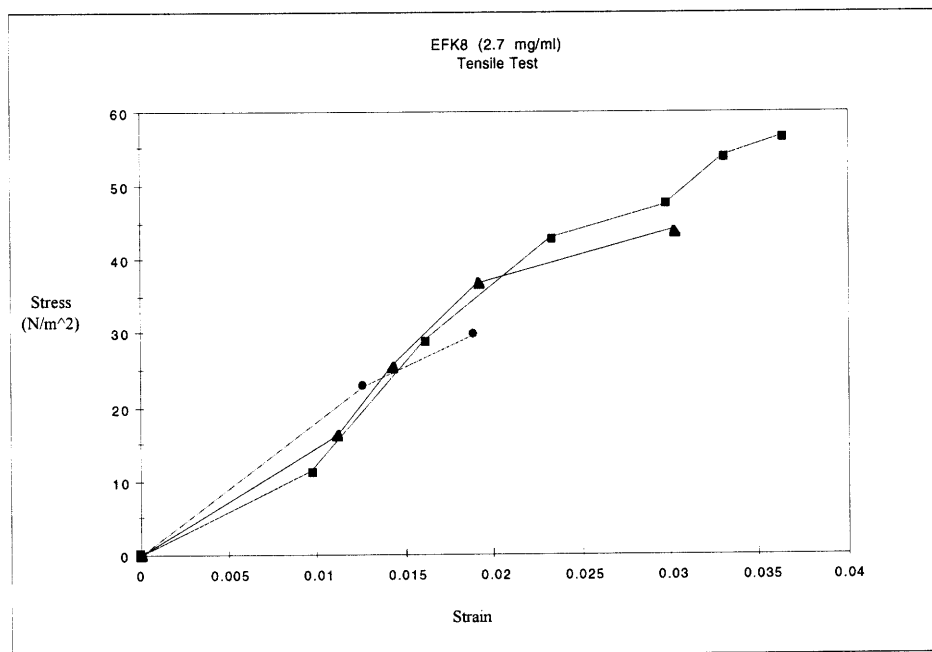


Figure 5.9. Tensile stress-strain curves for EFK8 at 2.7 mg/ml.

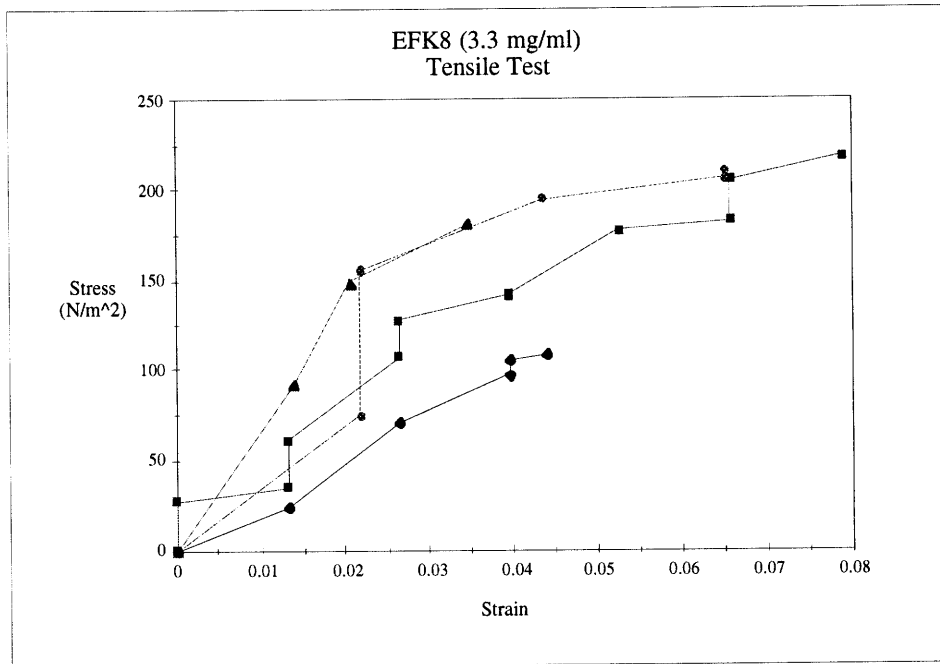


Figure 5.10. Tensile stress-strain curves for EFK8 at 3.3 mg/ml.

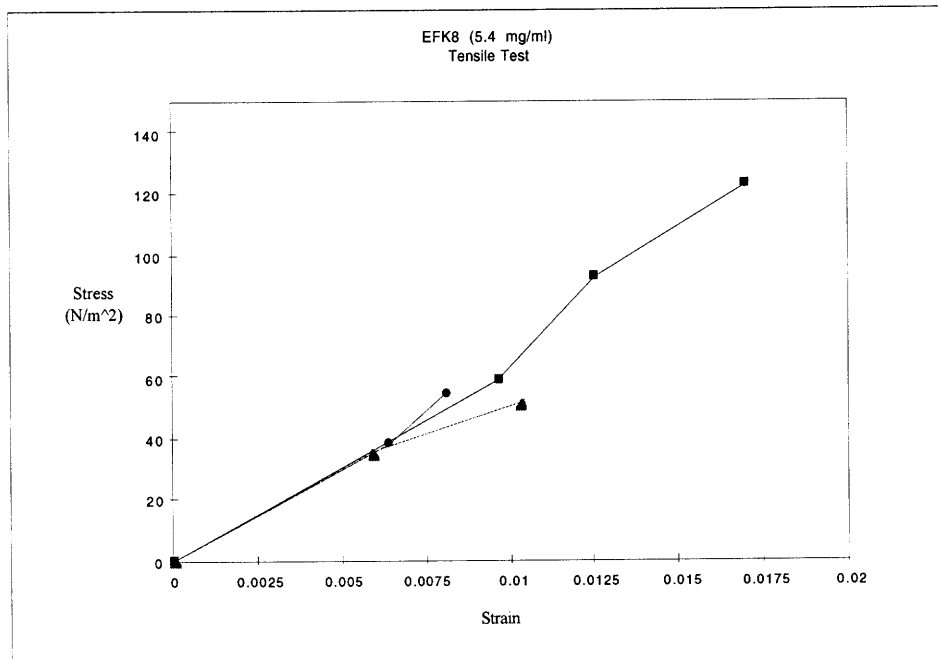


Figure 5.11. Tensile stress-strain curves for EFK8 at 5.4 mg/ml.

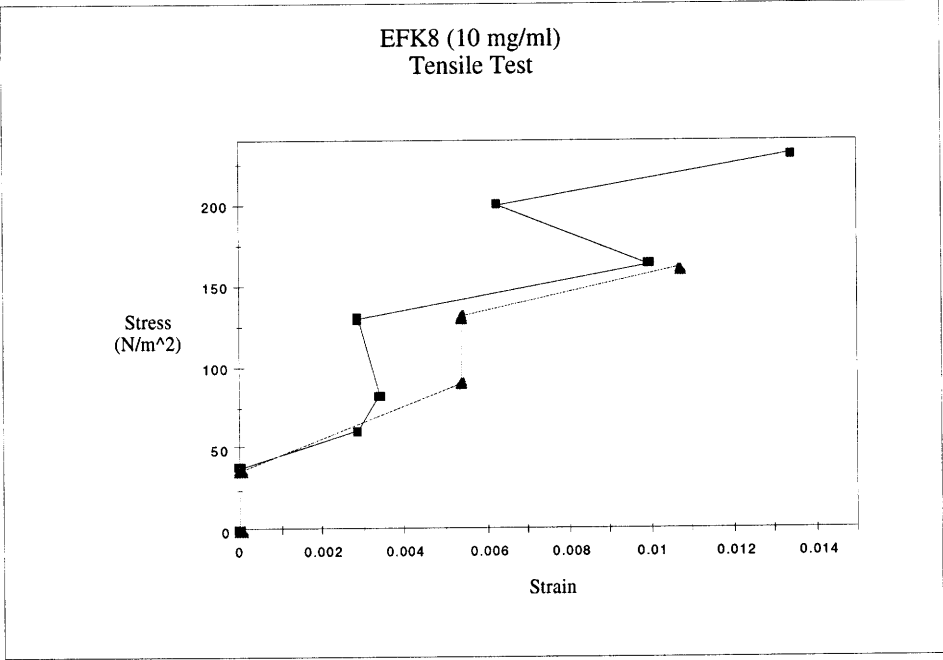


Figure 5.12. Tensile stress-strain curves for EFK8 at 10 mg/ml.

The variability in these data results from several sources of experimental error. As discussed in the specifications sections, testing hardware imposes resolution limitations that contribute to precision errors. Bias errors can be present due to system calibration errors. Furthermore, human error could be involved in the measurements. Variability in the data can also result from irregularities in the peptide materials. These can be introduced by side products of the chemical synthesis process of the peptides. The presence of small assembled or solidified aggregates in peptide solution can also affect specimen homogeneity. Differences in synthesis yields and levels of impurities in the peptides also play a factor in material variability.

5.6 References

1. Hayashi, K. "Mechanical Properties of Biomaterials: Relationship to Clinical Approach," *Contemporary Biomaterials*, New Jersey: Noyes Publications, 1984, pp. 46-65.
2. Ker, R.F. "Small-Scale Tensile Tests," *The Mechanical Properties of Biological Materials*, Cambridge: Cambridge University Press, 1980, pp. 487-489.
3. Aspden, R.M., T. Larson, R. Svensson, and D. Heingard. "Computer-Controlled Mechanical Testing Machine for Small Samples of Biological Viscoelastic Materials," *Journal of Biomedical Engineering*, 1991, Vol. 13, pp. 521-525.
4. Verma, N. "Design and Development of a Biomaterial Testing System," B.S. Thesis, MIT, 1996.

Chapter 6

Cellular Solid Analysis

6.1 Introduction

Cellular solids are materials whose structure consists of lattice-like networks of interconnected edges and walls. This type of structure has been observed in scanning electron micrographs of self-complementary oligopeptide materials. As a result, the theory of cellular solids was applied to the study of these materials. This theory relates the mechanical properties of the constitutive material, the mechanical behavior of the resulting network, and the geometrical characteristics of the cells.

This chapter presents some of the basic results from cellular solid theory. These results are used to analyze the mechanical properties data obtained from tensile experiments. The cellular theory is used in conjunction with these data to predict the properties of the solid fibers in the peptide materials and the dependence of network properties on concentration.

6.2 Background

The theory of cellular solids relates the mechanical properties of low density cellular materials to their structural characteristics (1). It can be used to describe the mechanical behavior of materials consisting of networks of interconnected fibers that form the edges of the staggered "cells." Gibson and Ashby have developed an analysis of the mechanical properties of open-celled materials from a model like the one depicted in Figure 6.1 (1). These unit cells are staggered with struts meeting at their midpoints. The analysis is based on a combination of basic mechanics and scaling ideas. When a cellular solid is stressed under tension or compression the fibers act like struts and beams. At low stresses the material behaves in a linearly-elastic manner. The deformation mechanism in this case consists of bending of the fibers or struts making up the cell edges. This deformation is illustrated in Figure 6.1b. At loads exceeding the linear-elastic regime, the struts buckle and plastic hinges are created (1). This leads to plastic collapse of the structure. If the

constitutive material is brittle, brittle crushing or brittle fracture are the cause of collapse (1).

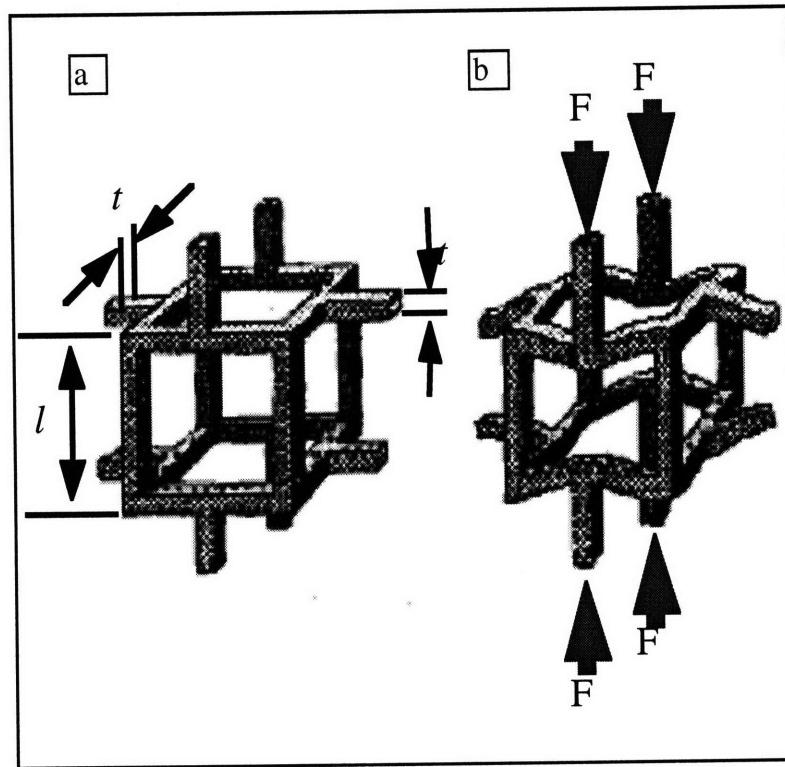


Figure 6.1. Unit cell model: a) undeformed and b) loaded and deformed by element bending. (Adapted from reference 1).

The unit cell model in Figure 6.1 has struts or fiber elements of length l and square cross section of thickness t . The relative density of the material is defined as the density of the network, ρ^* , divided by the density of the constitutive material ρ_s . As described in Chapter 4, this ratio depends on the geometry of the matrix structure. It is related to the cell dimensions t and l by

$$\frac{\rho^*}{\rho_s} \propto \left(\frac{t}{l}\right)^2 \quad (6-1)$$

(1). Beam theory (2) gives the deflection δ of a beam of length l subject to a force F acting at its midpoint as

$$\delta \propto \frac{Fl^3}{E_s I}, \quad (6-2)$$

where E_s is the stiffness of the beam constitutive material and I is the beam's second moment of area. This moment of area for a beam of square cross-section of side t is given by

$$I \propto t^4. \quad (6-3)$$

The stress σ is the force per unit area, or

$$\sigma \propto \frac{F}{l^2}. \quad (6-4)$$

The strain is related to beam the deflection δ by

$$\varepsilon \propto \frac{\delta}{l}. \quad (6-5)$$

Using the results from equations 6-2, 6-4, and 6-5, the network Young's modulus can be expressed as

$$E^* = \frac{\sigma}{\varepsilon} = \frac{CE_s I}{l^4} \quad (6-6)$$

where C is a constant of proportionality. Substituting equations 6-1 and 6-3 into 6-6 gives

$$\frac{E^*}{E_s} = C_1 \left(\frac{\rho^*}{\rho_s} \right)^2 \quad (6-7)$$

(1). Data from a wide range of materials and cell geometries give a value for C_1 of 1. A similar analysis for cellular materials subjected to shear stresses results in an expression for the network shear modulus G^* given by

$$\frac{G^*}{E_s} = C_2 \left(\frac{\rho^*}{\rho_s} \right)^2 \quad (6-8)$$

(1). The best fit of a large number of data for equation 6-8 gives a C_2 value of 3/8. If the material is linear-elastic and isotropic, elasticity theory (2) provides the following result

$$G = \frac{E}{2(1+\nu)}. \quad (6-9)$$

Substitution of the expressions for network moduli from equations 6-7 and 6-8 into 6-9 with the appropriate values of C_1 and C_2 results in an expression for the network Poisson's ratio ν^* of

$$\nu^* = \frac{1}{3} \quad (1). \quad (6-10)$$

Plastic collapse in open-cell materials occurs when the fully plastic moment of cell edges is exceeded by the moment resulting from the force F (1). Scaling analysis of this condition gives an expression for the plastic collapse σ_{pl}^* of

$$\frac{\sigma_{pl}^*}{\sigma_{ys}} = C_3 \left(\frac{\rho^*}{\rho_s} \right)^{3/2} \quad (1). \quad (6-11)$$

Brittle materials in tension fail by propagation of cracks. The scaling analysis of this deformation mechanism is done using the results of linear elastic fracture mechanics. It relates the network fracture toughness K^* to the solid toughness K_s by

$$\frac{K^*}{K_s} = C_4 \left(\frac{\rho^*}{\rho_s} \right)^{3/2} \quad (1). \quad (6-12)$$

Extensive data dictate the values of C_3 and C_4 as 0.3 and 0.65, respectively.

6.3 Analysis

The results from cellular solid theory can be used to estimate mechanical properties of the solid fibers that make up the oligopeptide materials. Equation 6-7 allows the calculation of the solid fibers' Young modulus from knowledge of the relative density and the matrix modulus. Relative density values are included in Chapter 4. The Young's moduli obtained from the tensile tests are presented in Chapter 5. For EFK8 at 3.3 mg/ml these data are

$$\frac{\rho^*}{\rho_s} = 0.01 - 0.04, \text{ and}$$

$$E^* = 2.90 \text{ kPa}.$$

Substitution of these values in 6-7 gives

$$E_s = 630E^* - 7870E^*, \text{ or}$$

$$E_s = 1.83 - 22.8 \text{ MPa}.$$

The data for EFK8 at 10 mg/ml give

$$\frac{\rho^*}{\rho_s} = 0.07 - 0.16, \text{ and}$$

$$E^* = 14.7 \text{ kPa}.$$

Substitution in 6-7 results in

$$E_s = 37.9E^* - 220E^*, \text{ or}$$

$$E_s = 0.56 - 3.23 \text{ MPa}.$$

The calculations of fiber modulus, E_s , are summarized in Table 6.1. Similar calculations were made for the fiber strength and are presented in Table 6.1

Table 6.1. Fiber Modulus Results: EFK8

Concentration (mg/ml)	ρ^*/ρ_s	E^* (kPa)	E_s (MPa)	σ_{fs}^* (Pa)	σ_{fs} (kPa)
3.3	0.01 - 0.04	2.90	1.83 - 22.8	176.3	33.8 - 272
10	0.07 - 0.16	14.7	0.56 - 3.23	196.5	4.7 - 163

The cellular solid analysis establishes the dependence of the network's mechanical properties on relative density. As discussed in Chapter 4, the relative density of the oligopeptide materials is proportional to their concentration. Therefore equation 6-7 can be rewritten in terms of the concentration M as

$$E^* = E_s B_1 (M)^2. \quad (6-13)$$

Combining the solid modulus and the proportionality constant B_1 into a single constant B_1 gives

$$E^* = B_1 (M)^2. \quad (6-14)$$

This expression indicates that the tensile modulus increases with the concentration. This trend was observed in the experimental data of EFK8. The data, which are presented in Chapter 5, are plotted to illustrate the concentration effect on matrix modulus. This plot is shown in Figure 6.2. A power law fit used for the data is given by

$$y = A(x)^n. \quad (6-15)$$

To fit the data of matrix modulus versus concentration, y must equal E^* when x equals M . The fit constant A gives B_1 while n should equal 2. The fit of the data gives A equal to 0.363 and n equal to 1.64. This results in a relation given by

$$E^* = 0.362(M)^{1.64} \quad (6-16)$$

where E^* is in kPa and M is in mg/ml. The data are also plotted on a logarithmic scale in Figure 6.3. This scale depicts power law relations, such as that in equation 6-15, as a line with slope equal to the exponent n . The power law fit is illustrated by a solid line in both the linear and the log-log scale. The error bars indicate uncertainty propagation from measurements, as discussed in Chapter 5.

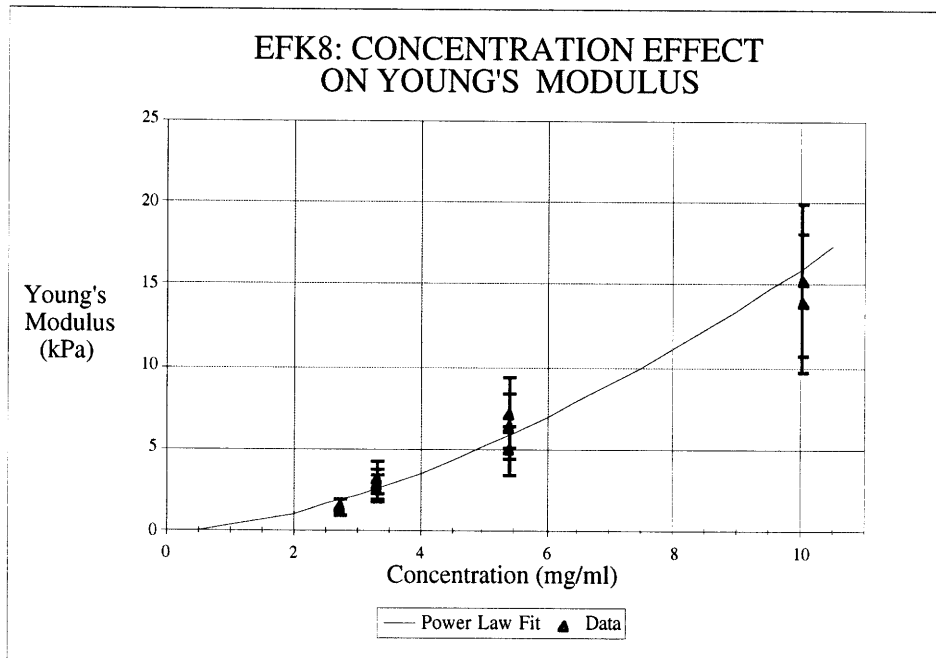


Figure 6.2. Young's moduli dependence on concentration for EFK8: linear scale.

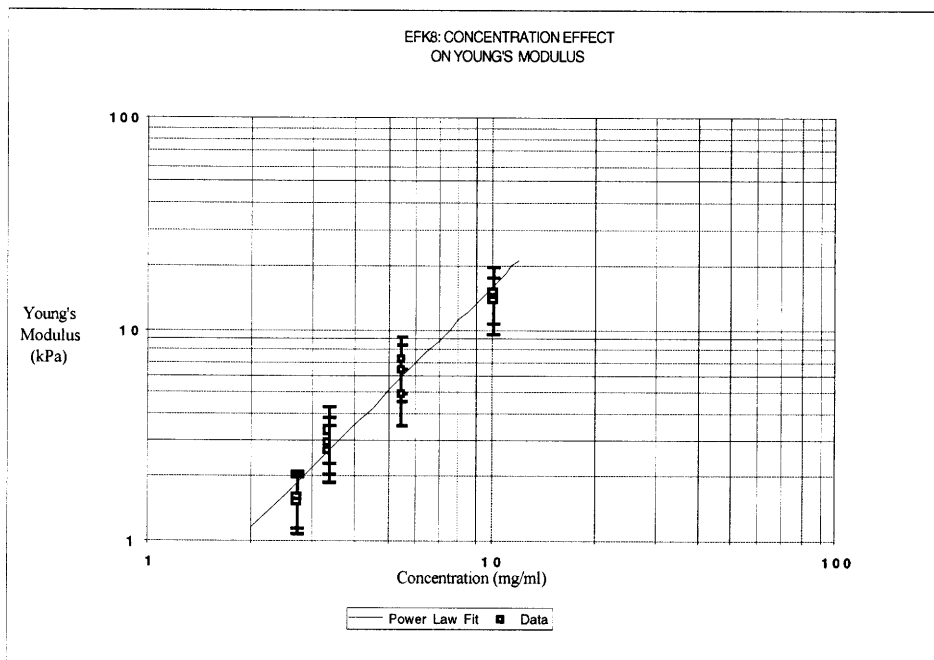


Figure 6.3. Young's moduli dependence on concentration for EFK8: logarithmic scale.

A similar analysis can be performed to characterize the concentration effect on the matrix fracture strength. The stress-strain curves for EFK8 exhibited linear behavior to fracture at the various concentrations tested. The peptide matrices behaved as a brittle-elastic material. Thus, brittle fracture is associated with the material failure. In this case, the fracture behavior should obey the fracture toughness relation of equation 6-12. This equation can be rewritten in terms of concentration M as

$$K^* = K_s B_2' (M)^{3/2}. \quad (6-17)$$

Since the toughness is proportional to the fracture strength, expression of this equation in terms of the matrix fracture strength, σ_{fs}^* , and the fiber strength, σ_{fs} , gives

$$\sigma_{fs}^* = \sigma_{fs} B_3' (M)^{3/2}. \quad (6-18)$$

Combining the fiber strength and the constant B_3' into B_3 results in

$$\sigma_{fs}^* = B_3 (M)^{3/2}. \quad (6-19)$$

The data for fracture strength versus concentration are plotted on linear and logarithmic scales in Figure 6.4 and Figure 6.5, respectively. These data were also fit using the power law form of equation 6-15. In this case, y equals σ_{fs}^* and x equals M . The fit constant A equals B_3 while the power law exponent, n , should equal 1.5. The fit on the data gives A equal to 56.3 and n equal to 0.573. The resulting relation has the form

$$\sigma_{fs}^* = 56.2 (M)^{0.572} \quad (6-20)$$

where σ_{fs}^* is in Pa and M is in mg/ml. The power law fit in equation 6-16 is depicted by a solid line in both the linear and the log-log scale.

The linear behavior of the material allows determination of elongation from the division of the stress by the modulus. Thus the strain at fracture is given by

$$\epsilon_f^* = \frac{\sigma_{fs}^*}{E^*}. \quad (6-21)$$

From the relations in equations 6-14 and 6-19, the dependence of ϵ_f^* on concentration, M , is given by

$$\epsilon_f^* = B_4 (M)^{-0.5} \quad (6-22)$$

where B_4 is a proportionality constant. This relation predicts a decrease in elongation at fracture with increase in concentration. This trend was observed in the data for EFK8. A plot of this relation is presented on linear scale and logarithmic scale in Figure 6.6 and

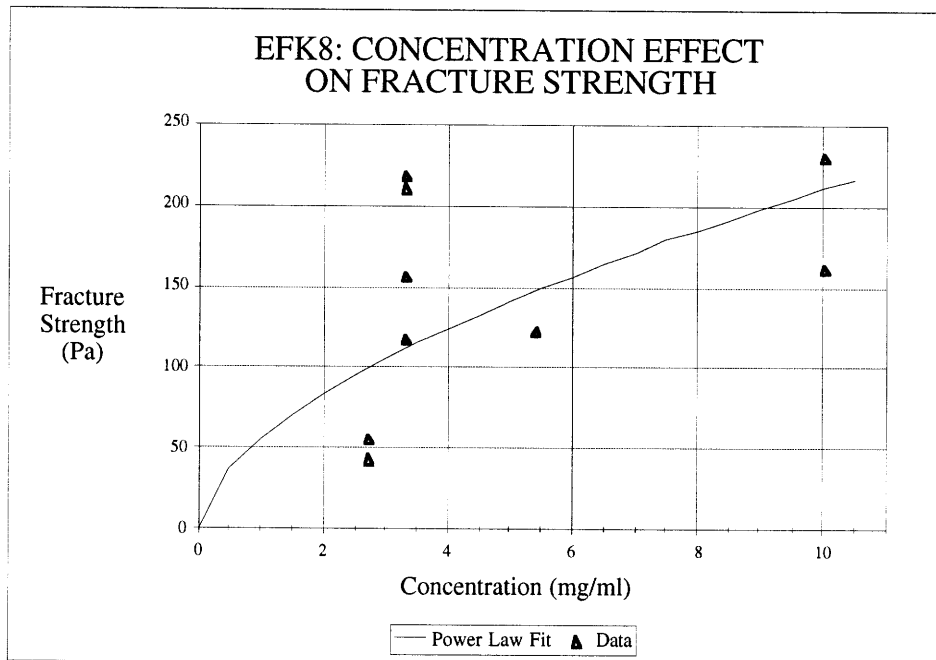


Figure 6.4. Fracture strength dependence on concentration for EFK8: linear scale.

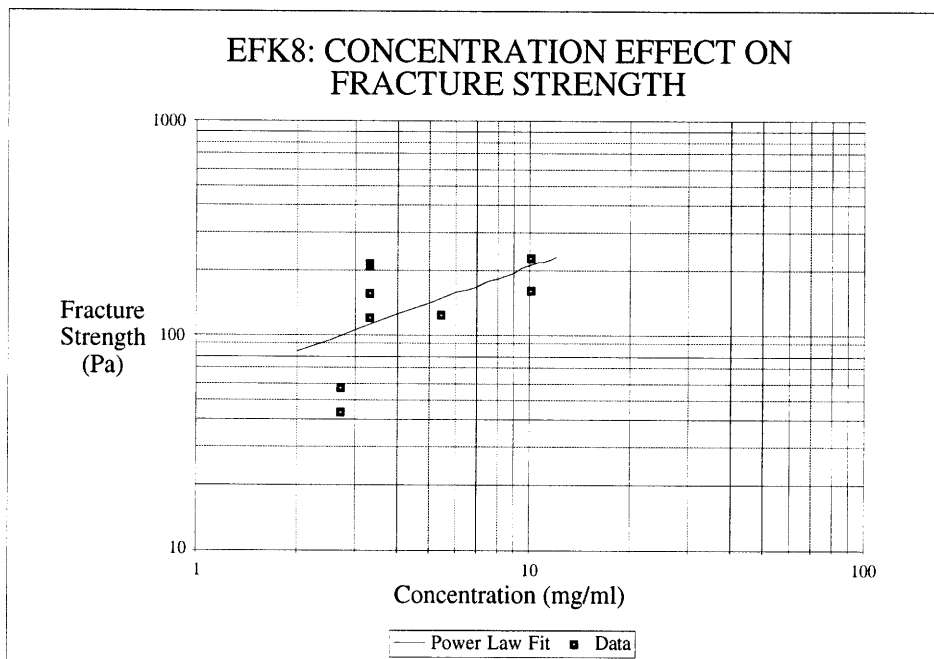


Figure 6.5. Fracture strength dependence on concentration for EFK8: logarithmic scale.

Figure 6.7, respectively. These data was fitted to the power law relation of equation 6-15. For this fit , y equals ϵ_f^* and x equals M . The resulting fit constant A equals B_4 and the power law exponent, n , should equal -0.5. The fit yields respective A and n values of 15.8 and -1.12. This result gives

$$\epsilon_f^* = 15.8(M)^{-1.12}, \quad (6-23)$$

which is represented by solid lines on Figure 6.6 and Figure 6.7. The error bars shown in these graphs indicate uncertainty in strain measurements due to resolution limitations. They do not account, however, for the inability to exactly locate the fracture point, as explained in Chapter 5.

6.4 Discussion

The mechanical test results for EFK8 demonstrated that its tensile properties are strongly dependent on concentration. The lattice-like structure of EFK8 motivated the use of cellular solids theory to model its behavior. The cellular solid analysis allows the use of the matrix Young's modulus and relative density to determine the modulus of the solid fibers. The data from EFK8 at 3.3 mg/ml give a predicted fiber modulus of 1.83 to 22.8 MPa. This result is expressed as a range due to the uncertainty in fiber thickness measurements, as discussed in Chapter 4. The data at 10 mg/ml give an estimate EFK8 fiber modulus of 0.56 to 3.23 MPa. The results from the two concentrations indicate different ranges but overlap in the 1.83 to 3.23 MPa. Therefore, there is a reasonable agreement between the calculations. Similar agreement was observed in the fiber tensile strength calculations. Data at 3.3 mg/ml predict a fiber strength of 33.8 to 272 kPa. The 10 mg/ml results give fiber strength of 4.7 to 163 kPa.

The experimental data showed that the matrix Young's modulus increases significantly with concentration. This observation is in agreement with the results from cellular solids theory. As indicated by equation 6-7, the network modulus increases as the square of the relative density. Since the relative density should be proportional to concentration, it is expected that modulus is proportional to the square of the concentration. A power law fit of the EFK8 data resulted in a power of 1.64 instead of 2, as indicated in equation 6-16. The fracture strength also increased with concentration. Cellular analysis indicates that the strength grows with the relative density in a power law form with an exponent of 1.5. The resulting data fit, equation 6-20, has a concentration to the power of 0.572.

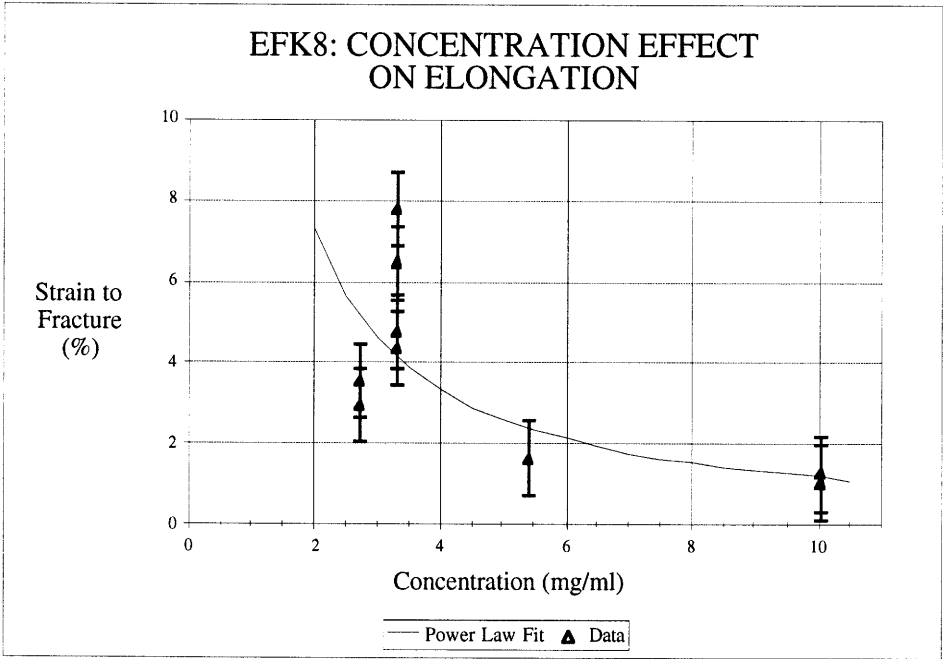


Figure 6.6. Elongation at fracture dependence on concentration for EFK8: linear scale.

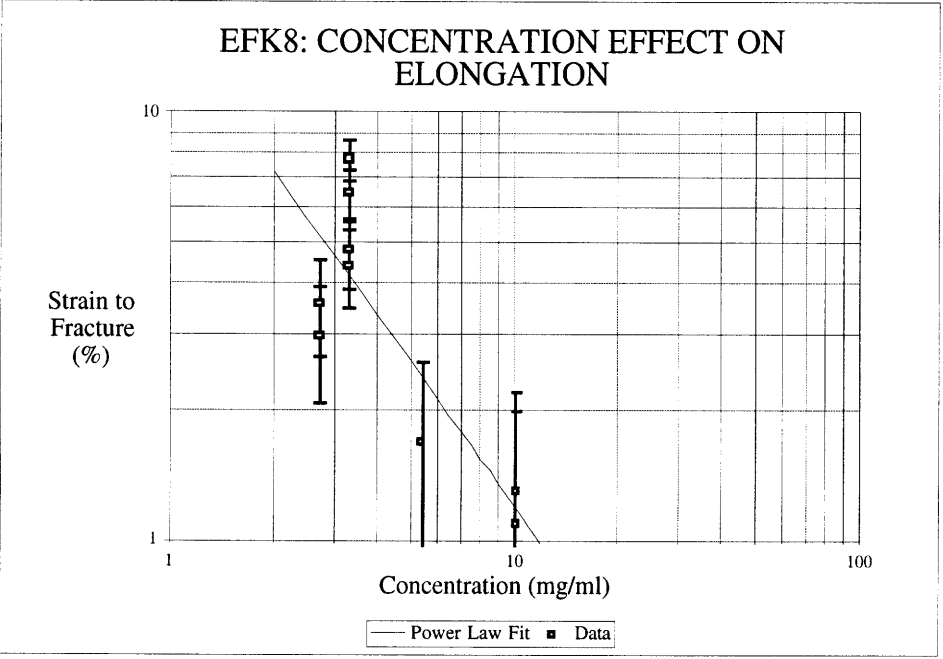


Figure 6.7. Elongation at fracture dependence on concentration for EFK8: logarithmic scale.

The data for both effects of concentration, namely Young's modulus and fracture strength, indicate power law exponents smaller than those predicted by theory. These slight deviations from the cellular solid behavior could be due to the nature of the material. The scanning electron micrographs of EFK8 matrices showed a lattice-like structure similar to those of cellular materials. However, the structure exhibited some irregularities and characteristics that depart from the simplifications made in cellular solid analysis. As evidenced in the micrographs, the oligopeptide material does not form perfectly regular or identical cells. Furthermore, the fibers show some curvature and corrugation. These structural aspects could have a significant impact but are not considered in the analysis. Another important structural aspect is the observed presence of material lumps at high concentrations. The clumping of material as concentration is increased would cause the relative density of the material to vary from cell to cell. Material sections where the relative density is lower will be weaker than the denser areas. These weaker areas will then be less stiff and fail at lower stresses. As a result the material stiffness and strength will exhibit increases with concentration smaller than those predicted by theory.

The linear behavior indicated by the stress-strain curves allows the determination of the elongation at fracture from the fracture strength and the Young's modulus. From this information and the cellular solids predictions, it was expected that the matrix strain at fracture would decrease with concentration in a power law form. Equation 6-22 shows the predicted relationship with fracture strain proportional to concentration raised to a power of -0.5. The EFK8 data showed the expected decrease in elongation with increase in concentration. However, the power law fit resulted in an exponent of -1.1 instead of -0.5. The exponent of -1.1 agrees with the data fits for Young's modulus and strength in equations 6-16 and 6-20. Using the two fit results instead of the theoretical predictions result in an expected power law exponent of -1.1.

Sources of experimental error also contribute to the discrepancy between theory predictions and tensile test data for EFK8. As discussed in Chapter 5, there are measurement errors resulting from the equipment resolution. Measurements of the exact stress and strain at fracture are difficult to obtain. Since the testing is done in fixed displacements, the fracture might occur during a displacement transition, making it hard to pinpoint the exact location of fracture in the stress-strain curve. Other sources of error result from the variability of the material. Irregularities in the material and its structure can introduce error in estimating the relative density from images. As discussed in Chapter 4, the measurements used for density calculations also introduce uncertainty to the data.

The tensile modulus for the EFK8 material ranged from 1.59 to 14.7 kPa for concentrations of 2.7 to 10 mg/ml. These values are comparable to those for collagen gels

and sponges at similar concentrations. Collagen sponge without cross-linking made from a 0.5-2% gel has an approximate modulus of 2.5 kPa (3). Collagen is a triple helix composed of three poly-peptide chains and is about 280 nm long (4, 5). The triple helix unit, termed tropocollagen, has an approximate molecular weight of 300,000 (4). EFK8, on the other hand, has a molecular weight of approximately 800 and a length of less than 6 nm. Thus, the EFK8 molecule is significantly smaller than tropocollagen but forms a material of comparable stiffness. The Young's modulus of the solid fibers in EFK8 is predicted to be between 0.56 and 22.8 MPa. These stiffness values are comparable to those of synthetic materials such as latex rubber and polybutadiene which have respective moduli of 2.6 MPa and 1 to 50 MPa (1).

6.5 References

1. Gibson, L. J. and M. F. Ashby. *Cellular Solids*. Pergamon Press, 1988.
2. Timoshenko, S.P. and J.N. Godier. *Theory of Elasticity, 3rd ed.* New York: McGraw-Hill, 1970.
3. Chvapil, M. "Collagen Sponge: Theory and Practice of Medical Applications," *Journal of Biomedical Materials Research*, Vol. 11, 1977, pp. 721-741.
4. Murabayashi, S., H. Kambic, and Y. Nose. "Reprocessed Biological Materials," *Encyclopedia of Material Science and Engineering*, Vol 6., 1986, pp. 4171-4178.
5. Calvert, P.D. "Biological Macromolecules," *Encyclopedia of Material Science and Engineering*, Vol. 1, 1986, pp. 327-339.